PHYSICAL REVIEW D VOLUME 45, NUMBER 11 1 JUNE 1992

Supersymmetric-Higgs-boson hadroproduction and decays including radiative corrections

V. Barger, M. S. Berger, and A. L. Stange
Physics Department, University of Wisconsin, Madison, Wisconsin 53706

R. J. N. Phillips
Rutherford Appleton Laboratory, Chilton, Didcot, Oxon, England
(Received 5 December 1991; revised manuscript received 12 March 1992)

Radiative corrections can produce substantial changes in the masses, production cross sections, and decay branching fractions of Higgs bosons in supersymmetric models, which can greatly modify their experimental detectability. We study variations in the expected event rates at pp supercolliders caused by radiative effects from the full one-loop effective potential in the minimal model, for the CP-even bosons h and H. We note that the masses of h, H, and the CP-odd boson A can simultaneously fall in the intermediate mass range $M_Z < m < 2M_Z$ that is difficult to explore at hadron supercolliders. We calculate the one-loop corrections to the triple neutral-Higgs-boson couplings that enter into the h and H branching fractions. We evaluate the $pp \to h(H)$ production cross sections at the Superconducting Super Collider energy, together with the principal h and H decay fractions, and compare them with standard-model results. We find that the h and H Higgs-boson signals in the $\gamma\gamma$ and $\ell^+\ell^-\ell^+\ell^-$ decay channels are generally less favorable than for the standard-model Higgs-boson search, except in some special cases.

PACS number(s): 14.80.Gt, 12.15.Cc, 13.85.Qk, 14.80.Ly

I. INTRODUCTION

A major impetus for the construction of new high-energy colliders is to determine whether Higgs bosons exist, as expected from the standard explanations of electroweak symmetry breaking. The most compelling theoretical framework incorporates supersymmetry (SUSY) to eliminate divergent contributions to the masses of scalar particles. The minimal supersymmetric standard model (MSSM) [1] has two complex Higgs doublets (H_1^0, H_1^-), (H_2^+, H_2^0); after spontaneous symmetry breaking, they give rise to two CP-even neutral Higgs bosons h, H (with $m_h < m_H$), a CP-odd neutral boson A, and two charged bosons $H^\pm$. At tree level, their masses and couplings are all closely interrelated, being specified by just two real parameters (e.g., the ratio of vacuum expectation values v_1, v_2 of the two Higgs doublets and the mass of one of the bosons). However, these predictions are subject to radiative corrections, first considered by Li and Sher [2]. It has recently been shown [3–10] that the tree-level Higgs-boson masses may suffer large one-loop corrections, with immediate consequences for the mass ranges that must be searched experimentally. Moreover, the couplings also suffer $O(g^2 m_t^4/M_W^4)$ corrections that change both the production cross sections and the decay branching fractions. The leading corrections modify the mixing angle α that specifies the neutral CP-even mass eigenstates and alters the triple Higgs-boson couplings. A realistic assessment of the discovery potential of MSSM Higgs bosons requires an evaluation of the importance of these corrections.

In this paper we shall study h and H signals at pp supercolliders, using the results for radiative corrections that have been derived using the effective potential formalism. The leading radiative corrections to the Higgs-boson masses and couplings are easily obtained in this method; the allowed mass ranges of the CP-even Higgs bosons are in general shifted upward. Large radiative corrections to the masses arise primarily because of a heavy top quark which induces corrections of $O(g^2 m_t^4/M_W^2)$ in the Higgs-boson self-energies. This mass shift is positive provided that the top squarks are heavier than the top quark. Other large corrections can arise when there exists significant mixing in the squark sector, and these mass shifts can be either positive or negative.

First we review the effective potential formalism and discuss its value as a means of approximating the radiatively corrected Higgs-boson masses. Then we proceed to discuss the correction to the Higgs-boson couplings, with the resulting changes in the hadroproduction cross sections, the decay branching fractions and the predicted signals.

Radiative corrections to MSSM Higgs-boson signals at e^+e^- colliders have previously been investigated in Refs. [7, 8]. The data from the CERN e^+e^- collider LEP have not yet received a complete MSSM analysis at the one-loop level, but preliminary indications are that the bound $m_h > 43\,\mathrm{GeV}$ can be set, with a weaker m_t-dependent bound on m_A [11]. Hadroproduced MSSM Higgs-boson signals have been studied at tree level in Ref. [12]; one-loop corrections have been incorporated for the first time in our present work. Our conclusions are summarized in Sec. VII. The bottom line is that the predicted h and H signals at pp supercolliders, in channels with amenable backgrounds, are generally much smaller than the corresponding SM Higgs boson signals; how-

ever, the MSSM signals equal or exceed SM values in some special cases.

II. EFFECTIVE POTENTIAL CALCULATIONS

A discussion of the effective potential [13] usually begins with a definition of the generating functional $W[J]$ which can be expanded in powers of the source J. The coefficients of each power are just the connected Green's functions. In the discussion that follows we will omit the indices on the scalar field. The generalization to the multicomponent case is straightforward. The classical field is defined as $\phi_c(x) \equiv \delta W/\delta J(x)$ and the effective action is defined as the Legendre transform of the generating functional

$$\Gamma[\phi_c] = W[J] - \int d^4x\, J(x)\,\phi_c(x)\,. \tag{1}$$

It can then be shown that the coefficients of the expansion of the effective action in powers of the classical field are the single-particle-irreducible (1PI) Feynman graphs

$$\Gamma^{(n)} = \left(\frac{\delta^n \Gamma[\phi_c]}{\delta \phi_c^n}\right)_{\phi_c = v}\,. \tag{2}$$

The effective action can also be expanded in powers of the momenta about the zero-momentum point

$$\Gamma[\phi_c] = \int d^4x\,[-V(\phi_c) + \tfrac{1}{2}(\partial_\mu \phi_c)^2 Z(\phi_c) + \ldots]\,. \tag{3}$$

$V(\phi_c)$ is called the effective potential and is the constant field piece of the effective action. By taking the Fourier transform of the effective action one obtains an expansion in terms of the transformed classical field. Then the effective potential can be expressed as a particular sum of the 1PI Feynman graphs evaluated at zero external momenta:

$$V(\phi_c) = -\sum_n \frac{1}{n!}(\phi_c - v)^n \tilde{\Gamma}^{(n)}(p=0)\,. \tag{4}$$

The tilde denotes the Fourier transform. In particular the second derivative of the effective potential is the two-point function with the external momentum equal to zero:

$$\tilde{\Gamma}^{(2)}(p=0) = -\left(\frac{\partial^2 V(\phi_c)}{\partial \phi_c^2}\right)_{\phi_c = v}\,. \tag{5}$$

The second derivatives of the tree-level scalar potential at its minimum are the squared masses of the scalar particles. This gives a mass squared matrix which can then be diagonalized to obtain the mass eigenstates. When one-loop corrections are added to the tree-level potential, it is no longer the case that the second derivatives define the physical masses of the scalar particles. Renormalization conditions can be defined for the effective potential that give finite values for these second derivatives, but these values are not the same as the zeros in the inverse matrix propagator which defines the physical Higgs-boson masses. The second derivatives of the effective potential are the 1PI Feynman diagrams with two external scalar lines evaluated with external momenta set to zero. The physical masses correspond to poles in these Feynman diagrams, so the relevant momenta at which to evaluate these diagrams is on shell. On the other hand, the effective potential can provide useful approximations to the physical Higgs-boson masses especially for the leading corrections in the MSSM.

In the MSSM there exist two complex Higgs doublets or a total of eight fields. The effective potential is a function of these eight fields and the renormalized Higgs-boson masses are obtained by taking the second derivatives of the effective potential with respect to these eight scalar fields, and evaluating the result at the potential minimum. The complexity of the couplings in the model however makes the resulting expressions lengthy.

At tree level the effective potential is just the scalar potential V_0 in the Lagrangian. At one loop there is an additional radiative contribution

$$\Delta V_1 = \frac{1}{64\pi^2}\mathrm{Str}\mathcal{M}(\phi_i)^4\left(\ln\frac{\mathcal{M}(\phi_i)^2}{\mu_R^2} - \frac{3}{2}\right)\,, \tag{6}$$

and the one-loop effective potential is $V_1(\phi_i) = V_0 + \Delta V_1$, μ_R is the renormalization scale, and the supertrace is defined as $\mathrm{Str} = \sum_J (-)^{2J}(2J+1)$. The masses $\mathcal{M}$ that appear in the effective potential are the field-dependent masses, and are expressed in terms of the classical modes of the theory ϕ_i. The radiative corrections can be calculated as an infinite sum of Feynman diagrams with external Higgs-boson lines. The lowest-order diagrams in this sum are shown in Fig. 1. The minimum of the potential occurs where $\partial V_1/\partial \phi_i = 0$ at which $\phi_i = v_i$. The Higgs-boson masses are obtained as the curvature at this minimum. The field-dependent masses depend upon contributions from the Higgs fields as well as field-

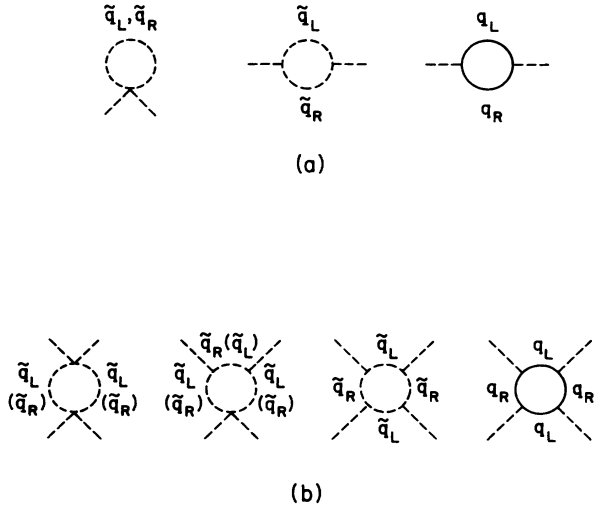

FIG. 1. The lowest-order diagrams contributing to the effective potential. The external lines are all possible Higgs fields (CP-even states, CP-odd states, and charged Higgs states) that can be added provided the couplings exist in the MSSM. The three-point coupling in the squark loop diagrams arises from mixing in the squark sector and changes a left eigenstate to a right eigenstate.

independent soft supersymmetry-breaking parameters.

The leading radiative effects come from one-loop diagrams involving squarks $\tilde{q}$ and the top quark t and involve additional mass parameters from the squark sector along with m_t. Since these scales are not known *a priori*, the consequences can only be explored qualitatively at present. Our considerations are based upon the full one-loop effective potential V_1, following Ref. [7]. Minimizing V_1 with respect to the Higgs fields determines the vacuum expectation values v_1, v_2 of H_1^0, H_2^0. The matrix of the second derivatives of V_1 with respect to the Higgs fields then gives an approximation to the radiatively corrected Higgs mass-squared matrix, that determines the physical Higgs-scalar masses and mixing angle. Some of the initial parameters can then be replaced by derived renormalized masses and expectation values. As independent parameters, we take m_A and $\tan\beta = v_2/v_1$, evaluated at one-loop order, together with m_t and the squark sector parameters m_Q, m_U, m_D, A_t, A_b, and μ (in the notation of Ref. [7]); here m_Q, m_U, m_D are soft supersymmetry-breaking squark masses, μ is the coefficient of the H_1H_2 mixing term in the superpotential, A_t and A_b are coefficients of trilinear $\tilde{t}_L\tilde{t}_RH_2$ and $\tilde{b}_L\tilde{b}_RH_1$ soft supersymmetry-breaking terms.

As a simple illustration we will derive the leading contribution to the effective potential from a heavy top quark taking $A_t = \mu = 0$. The field-dependent top-quark mass and top-squark masses are $m_t^2 = \lambda_t^2|H_2^0|^2$, $m_{\tilde{t}_L}^2 = \lambda_t^2|H_2^0|^2 + m_Q^2$ and $m_{\tilde{t}_R}^2 = \lambda_t^2|H_2^0|^2 + m_U^2$ where λ_t is the top Yukawa coupling. We have not included the dependence on the other Higgs fields nor the D-term contributions to $m_{\tilde{t}_L}^2$ and $m_{\tilde{t}_R}^2$ which do not contribute to the leading term of the effective potential at its minimum. The second derivative of the radiative correction with respect to the neutral CP-even fields ($\psi_i = \mathrm{Re}H_i^0, i = 1,2$) is

$$\frac{\partial^2\Delta V_1}{\partial\psi_i\partial\psi_j} = \frac{1}{32\pi^2}\mathrm{Str}\,\ln\frac{\mathcal{M}^2}{\mu_R^2}\left(\frac{\partial\mathcal{M}^2}{\partial\psi_i}\right)\left(\frac{\partial\mathcal{M}^2}{\partial\psi_j}\right) + \frac{1}{32\pi^2}\mathrm{Str}\mathcal{M}^2\left(\ln\frac{\mathcal{M}^2}{\mu_R^2} - 1\right)\left(\frac{\partial^2\mathcal{M}^2}{\partial\psi_i\partial\psi_j}\right). \tag{7}$$

For the case at hand the second term vanishes by the minimization conditions

$$\left(\frac{\partial\Delta V_1}{\partial\psi_i}\right)_{\psi_1=v_1,\psi_2=v_2} = 0. \tag{8}$$

Inserting the field-dependent masses into the first term and evaluating the resulting expression at the minimum, one obtains

$$\left(\frac{\partial^2\Delta V_1}{\partial\psi_2\partial\psi_2}\right)_{\psi_1=v_1,\psi_2=v_2} = \frac{(3)(2)}{8\pi^2}\lambda_t^2t^2\left(\ln\frac{\tilde{t}_L^2}{\mu_R^2} + \ln\frac{\tilde{t}_R^2}{\mu_R^2} - 2\ln\frac{t^2}{\mu_R^2}\right). \tag{9}$$

where for compactness we use the notation X^2 for m_X^2. The 3 is a color factor and there is a factor of 2 because the particles are not self-conjugate. The μ_R^2 dependence cancels and we arrive at the result

$$\left(\frac{\partial^2\Delta V_1}{\partial\psi_2\partial\psi_2}\right)_{\psi_1=v_1,\psi_2=v_2} = \frac{3t^4g^2}{8\pi^2W^2\sin^2\beta}\ln\left(\frac{\tilde{t}_L^2\tilde{t}_R^2}{t^4}\right). \tag{10}$$

This is the leading term, contributing to 2× the mass-squared matrix (due to the normalization of H_1^0 and H_2^0). The complete expression is derived in Ref. [7].

We proceed as follows. First, values of m_A and $\tan\beta$ are selected; this determines the quantity

$$\Delta = m_A^2\sin 2\beta, \tag{11}$$

that appears subsequently in the mass-squared matrix for the CP-even Higgs scalars. Next, the four eigenvalues $\tilde{t}_1^2$, $\tilde{t}_2^2$, $\tilde{b}_1^2$, $\tilde{b}_2^2$ of the $\tilde{t}$ and $\tilde{b}$ mass-squared matrices are determined; their values are

$$\tilde{t}_i^2 = t^2 + \tfrac{1}{2}(Q^2+U^2) + \tfrac{1}{4}Z^2\cos 2\beta \pm\{[\tfrac{1}{2}(Q^2-U^2) + \tfrac{1}{12}(8W^2-5Z^2)\cos 2\beta]^2 + t^2(A_t+\mu\cot\beta)^2\}^{1/2}, \tag{12a}$$

$$\tilde{b}_i^2 = b^2 + \tfrac{1}{2}(Q^2+D^2) - \tfrac{1}{4}Z^2\cos 2\beta \pm\{[\tfrac{1}{2}(Q^2-D^2) - \tfrac{1}{12}(4W^2-Z^2)\cos 2\beta]^2 + b^2(A_b+\mu\tan\beta)^2\}^{1/2}. \tag{12b}$$

The masses m_h, m_H and mixing-angle α in the CP-even Higgs sector are then determined by diagonalizing the mass-squared matrix [7]:

$$\frac{1}{2}\begin{pmatrix}\cot\beta & -1\\ -1 & \tan\beta\end{pmatrix}Z^2\sin 2\beta + \frac{1}{2}\begin{pmatrix}\tan\beta & -1\\ -1 & \cot\beta\end{pmatrix}\Delta + \frac{3g^2}{16\pi^2W^2}\begin{pmatrix}\Delta_{11} & \Delta_{12}\\ \Delta_{12} & \Delta_{22}\end{pmatrix} \tag{13}$$

in the basis $\phi_1 = \sqrt{2}(\psi_1 - v_1)$, $\phi_2 = \sqrt{2}(\psi_2 - v_2)$; the mixing angle α is defined by

$$h = \phi_2\cos\alpha - \phi_1\sin\alpha, \quad H = \phi_1\cos\alpha + \phi_2\sin\alpha. \tag{14}$$

Here the entries Δ_{ij} are defined in terms of parameters that characterize mixing in the squark sector,

$$C_b = (A_b + \mu\tan\beta)/(\tilde{b}_1^2 - \tilde{b}_2^2), \tag{15a}$$

$$C_t = (A_t + \mu\cot\beta)/(\tilde{t}_1^2 - \tilde{t}_2^2), \tag{15b}$$

and a loop factor

$$g_q = 2 - (\tilde{q}_1^2 + \tilde{q}_2^2)\ln(\tilde{q}_1^2/\tilde{q}_2^2)/(\tilde{q}_1^2 - \tilde{q}_2^2), \tag{16}$$

by the formulas

$$\Delta_{11} = \frac{t^4}{\sin^2\beta} g_t C_t^2 \mu^2 + \frac{b^4}{\cos^2\beta}\left\{\ln\left(\frac{\tilde{b}_1^2\tilde{b}_2^2}{b^4}\right) + A_b C_b\left[2\ln\left(\frac{\tilde{b}_1^2}{\tilde{b}_2^2}\right) + A_b C_b g_b\right]\right\}, \tag{17a}$$

$$\Delta_{22} = \Delta_{11} \quad \left(\text{with } t \leftrightarrow b,\ \tilde{t} \leftrightarrow \tilde{b},\ \beta \rightarrow \frac{\pi}{2} - \beta\right), \tag{17b}$$

$$\Delta_{12} = \frac{t^4}{\sin^2\beta}\mu C_t\left[\ln\left(\frac{\tilde{t}_1^2}{\tilde{t}_2^2}\right) + A_t C_t g_t\right] + \left(t \leftrightarrow b,\ \tilde{t} \leftrightarrow \tilde{b},\ \beta \rightarrow \frac{\pi}{2} - \beta\right). \tag{17c}$$

We follow the standard conventions that v_1 and v_2 are positive, $0 \leq \beta \leq \pi/2$ and $-\pi/2 \leq \alpha \leq 0$. The trace $\Delta_{11}+\Delta_{22}$ agrees with the leading terms in the expression obtained in Ref. [4] in the limit of vanishing Higgs-boson masses; this limit corresponds precisely to the effective potential approximation.

We note that radiative corrections to the tree-level mass sum rule

$$m_h^2 + m_H^2 = m_A^2 + m_Z^2, \tag{18}$$

arising from the trace $\Delta_{11} + \Delta_{22}$ in the third term of Eq. (13), can be large only for large values of A_q and μ [3, 4] or if m_t is large [4]. It is exactly these large corrections that have also been considered more recently for the individual Higgs-boson masses. The soft squark mass parameters m_Q, m_U, and m_D, decouple from the sum rule in the limit that they become very large.

A check on the validity of the effective potential approximation is possible since the corrections to the sum rule have been calculated in a diagrammatic fashion with the external Higgs bosons put on shell and the poles in the propagator identified. In the corrections to the sum rules the familiar two-point integrals of the form

$$\int_0^1 dx \ln\left[x m_1^2 + (1-x)m_2^2 - x(1-x)m_3^2\right] \tag{19}$$

occur where m_1 and m_2 are the masses of virtual particles circulating in the loop and m_3 is the mass of the external leg. The effective potential approximates this integral by setting $m_3 = 0$. For the case $m_1 = m_2$ the largest deviation occurs just at the threshold $m_3 = 2m_1$, above which the integral develops an imaginary part as the external particle becomes unstable to decay into real on-shell particles. We find that the corrections to the trace $\Delta_{11} + \Delta_{22}$ for the case $A_t = \mu = 0$ are only a few percent for $\tan\beta > 10$. For smaller values of $\tan\beta$ the correction can be larger as the heavier Higgs boson H becomes relatively more important in the extrapolation to on shell. For example, the correction can be as large as 15% near the threshold $m_H = 2m_t$ if $\tan\beta = 2$. Figure 2 shows the ratio of the radiative correction from the exact expression in Ref. [4] to that obtained in the effective potential approximation, for three values of $\tan\beta$.

If the Yukawa couplings of b and t are comparable then $\tan\beta$ is of order m_t/m_b; for $m_t = 150\,\text{GeV}$ this would give $\tan\beta \approx 30$. In the large $\tan\beta$ limit, the CP-even mass-squared matrix becomes diagonal, both at the tree level and at one-loop level, and one eigenvalue equals m_A. An additional U(1) symmetry in the limit of large $\tan\beta$ and small squark mixing gives rise to this mass degeneracy [6]. The second eigenvalue equals M_Z in tree approximation, but with radiative corrections it becomes

(for $A_t = \mu = b^2 = 0$)

$$m_{\text{Higgs}}^2 = M_Z^2 + \frac{3g^2}{16\pi^2 W^2}\Delta_{22} = M_Z^2 + \frac{3}{\pi^2}\frac{G_F}{2\sqrt{2}} t^4 \ln\left(\frac{\langle\tilde{t}^2\rangle^2}{t^4}\right), \tag{20}$$

where $\langle\tilde{t}^2\rangle = \tilde{t}_1\tilde{t}_2$ is the mean top-squark squared mass. The contributions of the bottom quarks explicitly break the global U(1) symmetry, but these corrections are in general small. In the large $\tan\beta$ limit the bottom-quark corrections become relatively more important, but even for $\tan\beta \approx m_t/m_b$ they are still suppressed relative to the top-quark contributions and we neglect them temporarily. (Of course if β is exactly $\pi/2$ then the bottom-quark Yukawa coupling must be infinite, and the correction then is infinite.) The mixing angle in the large $\tan\beta$ limit is either $\alpha = 0$ or $\alpha = -\pi/2$, for m_A^2 less than or greater than $M_Z^2 + \Delta_{22}$, respectively.

For $m_t = 150\,\text{GeV}$ and $m_{\tilde{t}_1} \simeq m_{\tilde{t}_2} \simeq 1\,\text{TeV}$, the numerical value of the fixed eigenvalue above is

$$m_{\text{Higgs}}^2 = M_Z^2 + \frac{3g^2}{16\pi^2 W^2}\Delta_{22} \simeq (115\,\text{GeV})^2, \tag{21}$$

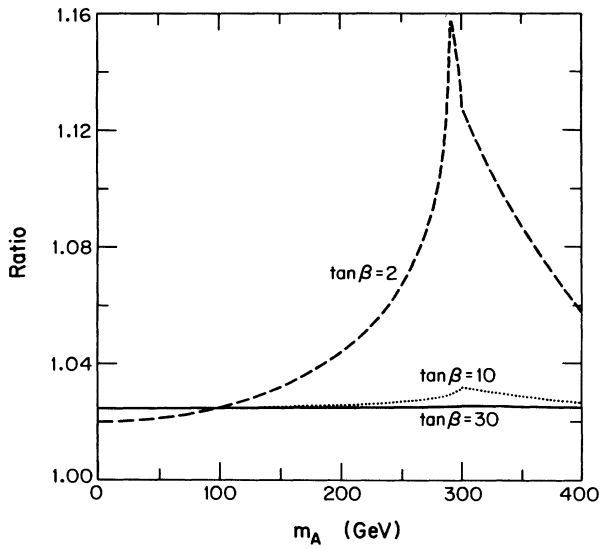

FIG. 2. A test of the effective potential approximation: the ratio of the exact one-loop correction in the neutral mass sum rule to that obtained from the effective potential approximation is shown vs m_A for $\tan\beta = 2$, 10, 30 with $A_t = \mu = 0$ and $m_t = 150\,\text{GeV}$. The loop integrals are entirely real until Higgs-boson masses are increased beyond the thresholds $m_H = 2m_t$ and $m_A = 2m_t$. For large values of $\tan\beta$ these two thresholds almost coincide.

and it is therefore natural to expect one of the masses to be of this order if $m_t \sim 150\,\mathrm{GeV}$ and $\tan\beta$ is large. In fact the fixed eigenvalue is a lower bound of m_H and an upper-bound of m_h for any $\tan\beta$ if we neglect squark mixing. Figure 3 shows this fixed mass eigenvalue versus m_t for mean stop mass scales 1 and 0.5 TeV. The other CP-even eigenstate is degenerate in mass with the CP-odd eigenstate A. To summarize, for large $\tan\beta$ two of the neutral-Higgs-boson masses are degenerate, the third mass is determined by the top and stop masses and the mass-squared sum rule becomes

$$m_h^2 + m_H^2 = m_A^2 + M_Z^2 + \frac{3g^2}{16\pi^2 W^2}\Delta_{22}\,. \tag{22}$$

If we now let A_t be nonzero keeping $\mu = 0$, then the mass degeneracy of two of the Higgs bosons is preserved, but the mass of the third receives an additional correction since

$$\Delta_{22} = t^4 \ln\left(\frac{\langle\tilde{t}^2\rangle^2}{t^4}\right) + t^4 A_t C_t \left[2\ln\left(\frac{\tilde{t}_1^2}{\tilde{t}_2^2}\right) + A_t C_t g_t\right]\,. \tag{23}$$

As long as A_t is not too large, the mixing in the top-squark mass matrix is small and this correction is also small. For example, if we choose the soft mass parameters $m_Q \simeq m_U \simeq m_D \simeq 1\,\mathrm{TeV}$ and take $A_t \simeq 0.5\,\mathrm{TeV}$ we get only a few GeV correction to the value of the Higgs-boson mass obtained when $A_t = 0$.

If both A_t and μ are nonzero, the degeneracy of a CP-even Higgs boson with the CP-odd Higgs boson is broken by the combined effects of mixing in the squark mass matrices and the Higgs-boson–squark–squark couplings. Again if μ is not too large, the corrections to the Higgs-boson masses are not large.

The charged-Higgs-boson mass $m_{H^\pm}$ is modified by the one-loop contributions but its couplings to gauge bosons and fermions are unchanged in the effective potential approximation. Like the CP-odd states, the charged-Higgs-boson mass-squared matrix is diagonalized by a rotation determined by the angle β. At tree level $m_{H^\pm}^2 = m_A^2 + m_W^2$, and the radiatively corrected formulas for $m_{H^\pm}$ are given in Ref. [7]. The charged-Higgs-boson mass-squared matrix is described by an expression analogous to Eq. (13):

$$\frac{1}{2}\begin{pmatrix}\tan\beta & 1\\ 1 & \cot\beta\end{pmatrix} W^2 \sin 2\beta + \frac{1}{2}\begin{pmatrix}\tan\beta & 1\\ 1 & \cot\beta\end{pmatrix}\Delta + \frac{1}{2}\begin{pmatrix}\tan\beta & 1\\ 1 & \cot\beta\end{pmatrix}\tilde{\Delta}\sin 2\beta \tag{24}$$

One eigenvalue is zero corresponding to the charged Goldstone boson. The radiative corrections to the physical charged Higgs boson are expressed as corrections to the tree-level sum rule as $m_{H^\pm}^2 = m_A^2 + m_W^2 + \tilde{\Delta}$. For $m_Q \simeq m_U \simeq m_D \simeq 1\,\mathrm{TeV}$ and $A_t \simeq 0.5\,\mathrm{TeV}$, $\mu \simeq 0.25\,\mathrm{TeV}$ we find that the radiative corrections are well approximated by neglecting A_t and μ in which case

$$\tilde{\Delta} = \frac{3g^2}{64\pi^2 \sin^2\beta\cos^2\beta W^2} \times\left(\frac{(b^2 - W^2\cos^2\beta)(t^2 - W^2\sin^2\beta)}{\tilde{t}_1^2 - \tilde{b}_1^2}[f(\tilde{t}_1^2) - f(\tilde{b}_1^2)] + \frac{t^2 b^2}{\tilde{t}_2^2 - \tilde{b}_2^2}[f(\tilde{t}_2^2) - f(\tilde{b}_2^2)] - \frac{2t^2 b^2}{t^2 - b^2}[f(t^2) - f(b^2)]\right), \tag{25}$$

where $f(m^2) = 2m^2[\ln(m^2/\mu_R^2) - 1]$. We choose $\mu_R^2 = W^2$ as the renormalization scale. This relatively simple expression gives values which agree within about 5% with those obtained from the exact expression for $\tan\beta > 1$ (and so the radiatively corrected $H^\pm$ mass is accurate to within 1%). Notice that the leading corrections to the charged-Higgs-boson mass are proportional to t^2 or to $t^2 b^2/W^2$ as opposed to t^4/W^2 in the neutral Higgs case. The corrections to the charged-Higgs-boson mass are generally smaller than the corrections to the CP-even Higgs boson.

Concrete examples of these one-loop radiative mass shifts are given in the following section.

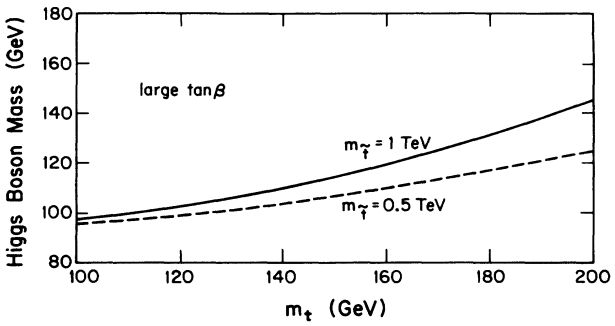

FIG. 3. The mass of the CP-even eigenstate that is approximately independent of m_A for large $\tan\beta$, is shown vs m_t for mean stop mass 1 TeV (solid curve) and 0.5 TeV (dashed curve). The other CP-even eigenstate has mass m_A for large $\tan\beta$.

III. NEUTRAL-HIGGS-BOSON COUPLINGS

Previous studies have focused on the radiative corrections to the Higgs-boson masses [2–10] and the ZZh, ZhA couplings [7, 8] that determine $e^+e^- \to hZ, hA$ production at LEP. Here we explore more generally the couplings of neutral CP-even Higgs bosons that control their production at hadron colliders and their decay branching fractions. Radiative corrections enter here through the mixing angle α (the couplings of A and $H^\pm$ do not depend on α and are thus not affected by this source of corrections) and in modifications to the triple Higgs-boson couplings. Not only the couplings to W and

Z gauge bosons but also the Higgs-boson couplings to heavy quarks are important here. The α and β dependences of these couplings are given by the factors

	$t\bar{t}$	$b\bar{b}, \tau^+\tau^-$	WW, ZZ
h	$\cos\alpha/\sin\beta$	$-\sin\alpha/\cos\beta$	$\sin(\beta-\alpha)$
H	$\sin\alpha/\sin\beta$	$\cos\alpha/\cos\beta$	$\cos(\beta-\alpha)$.

(26)

The corresponding terms in the Lagrangian are multiplied by the standard-model Higgs couplings $-(\sqrt{2}G_F)^{1/2}m_q$ for quarks, $(\sqrt{2}G_F)^{1/2}2M_W^2$ for W, and $(\sqrt{2}G_F)^{1/2}M_Z^2$ for Z.

In hadroproduction we encounter Higgs-boson couplings to gg, WW, ZZ, and $t\bar{t}$; further couplings to $\gamma\gamma$, $c\bar{c}$, $b\bar{b}$, $\tau\bar{\tau}$ enter the calculation of decay branching fractions. In our concrete illustrations we take a common SUSY mass scale

$$m_Q = m_U = m_D \equiv m \tag{27}$$

and set

$$A_t = A_b = 2\mu = m/2 , \tag{28}$$

such that squark mixing is present but not overwhelming. We shall present illustrations of the corrections to individual Higgs-boson masses and couplings using the choices

$$m_t = 150\,\text{GeV} , \quad m = 1\,\text{TeV} . \tag{29}$$

Now for given values of m_A and $\tan\beta$, all the Higgs-boson masses and the mixing angle α are determined and the fermion couplings are given in terms of α and β. In place of m_A, we can equally well use the mass of whichever Higgs boson is of immediate interest.

Figure 4 shows results for the radiatively corrected masses m_h, m_H, and $m_{H^\pm}$ versus m_A for the two choices $\tan\beta = 2$ (dashed curves) and $\tan\beta = 30$ (solid curves), along with the tree-level results for comparison. This illustrates that the ranges $m_h > M_Z$ and $m_{H^\pm} < M_W$, forbidden at tree level, can be realized after radiative corrections. It may be significant that for large $\tan\beta$ the masses of all three neutral Higgs bosons h, H, and A can simultaneously fall in the intermediate-mass region between M_Z and $2M_Z$ that is difficult to explore at hadron supercolliders. Finally, we recall that parameter sets giving $m_h < 43\,\text{GeV}$ appear to be already excluded by LEP data [11]; depending on $\tan\beta$, this implies the exclusion of certain ranges of m_A, m_H, and $m_{H^\pm}$ near their lower end points [see Figs. 4(b) and 4(c)].

Figure 5 gives the dependence of the mixing angle α on m_h, m_H or m_A, again for $\tan\beta = 2$ and $\tan\beta = 30$. Here the radiatively corrected results (solid curves) are compared with tree-level results (dotted curves). With our SUSY parameter choices, the one-loop corrections can give big shifts in α that produce correspondingly important shifts in the couplings (even larger effects would be obtained with $m_t = 200\,\text{GeV}$). We note that α is systematically shifted to larger, more negative values, for given m_h or m_H; this appears to be generally the case for a wide range of SUSY parameter values. The effects on the couplings can be read directly from Eq. (26). Thus we see that the $hb\bar{b}$ and $h\tau^+\tau^-$ couplings are enhanced, the $ht\bar{t}$ coupling is reduced, and for large $\tan\beta$ ($\beta \simeq \pi/2$) the hWW and hZZ couplings are also reduced; each corresponding H coupling is shifted in the opposite direction.

It is also interesting to note the end-point values of α for given $\tan\beta$.

(i) As $m_A \to \infty$ (and $m_h \to$ its upper bound) we have $\alpha \to \beta - \pi/2$ both at tree level and in general; in this limit we recover precisely the SM couplings for h, while H and A become very heavy and largely irrelevant. When a Higgs-boson mass becomes large in the MSSM it decouples from the gauge bosons since its mass is being driven by large SU(2) × U(1)-invariant masses.

(ii) As $m_A \to 0$ (and $m_H \to$ its lower bound) we have $\alpha \to -\beta$ at tree level, with a radiative correction to α downwards; at tree level the $Ht\bar{t}$ and the $Hb\bar{b}$ coupling reduce in this limit to the SM values within a sign, while the HWW and HZZ couplings reduce to $\cos 2\beta$ times the SM value. With the radiative correction to α, the $Ht\bar{t}$ coupling is shifted to a slightly larger value, and the $Hb\bar{b}$ coupling is shifted to a slightly smaller value. Assuming moderate-to-large $\tan\beta$, the H couplings reduce approximately to SM values within a sign while the h couplings are mostly suppressed (except $hb\bar{b}$ and $h\tau^+\tau^-$). For given $\tan\beta$, the LEP bound $m_h > 43$ GeV excludes

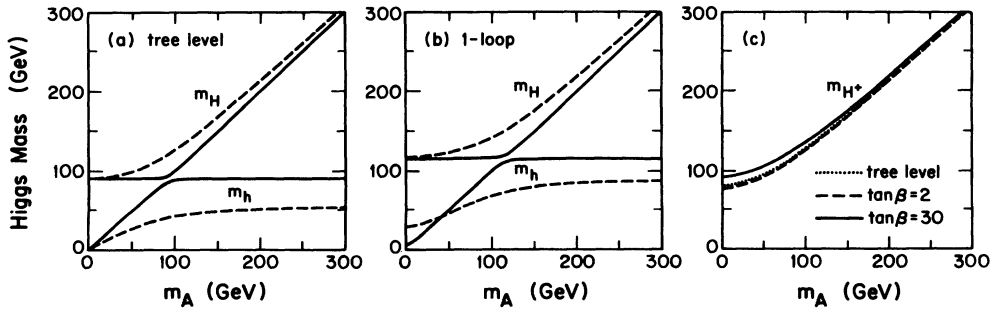

FIG. 4. Typical results for Higgs-boson masses, with and without radiative corrections, vs the input mass m_A for $\tan\beta = 2$ (dashed curves) and $\tan\beta = 30$ (solid curves): (a) m_h and m_H at tree level, (b) m_h and m_H at one-loop level, and (c) $m_{H^\pm}$ at tree and one-loop level.

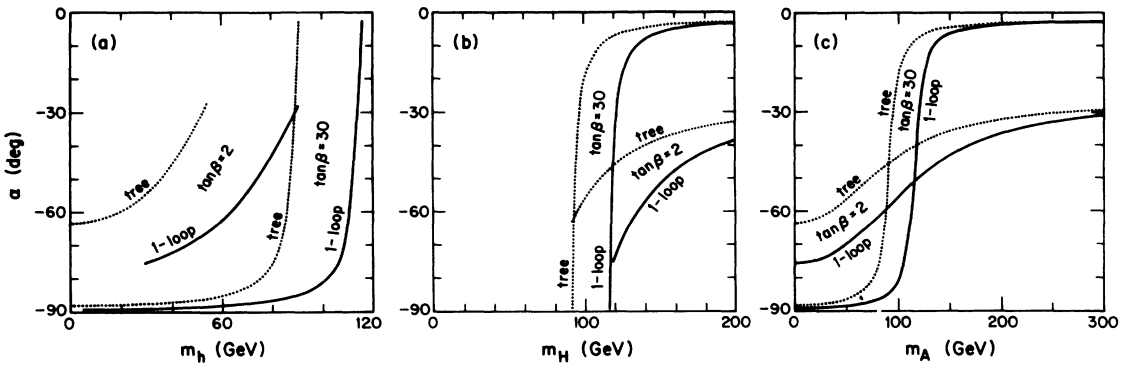

FIG. 5. The mixing angle α in the CP-even Higgs-boson sector is shown vs (a) m_h, (b) m_H, and (c) m_A for $\tan\beta = 2$ and $\tan\beta = 30$. Solid curves denote the radiatively corrected values of α, dotted curves represent tree-level results.

a small range of m_H near its lower end point; however, we see from Fig. 5(a) that the end-point value of α can still be approached so that part of this end-point region is still allowed.

Because m_h, m_H, and α all depend very nonlinearly on the input parameter m_A, Figs. 5(a) and 5(b) give the impression that these end-point regions (where either $\alpha \simeq \beta - \pi/2$ or $\alpha \simeq -\beta$) may occupy only a small part of parameter space. In Fig. 5(c) however, where α is plotted versus m_A instead, we see that the end-point regions of α occupy a substantial part of parameter space (especially for large $\tan\beta$); it therefore seems not unlikely that such values of α should be realized.

In a complete analysis, the vertex corrections also have to be calculated to obtain the full one-loop corrections to the couplings. The corrections to the mixing angle α and to the triple Higgs-boson couplings are $O(g^2 m_t^4/M_W^4)$ and are included in our analysis. The other vertex corrections are only $O(g^2 m_t^2/M_W^2)$ and are neglected.

New non-SM decays which will be kinematically possible for some regions of parameter space are $H \to hh, AA, ZA$ and $h \to AA$ (we neglect the decays which are higher order in perturbation theory such as $H \to hhh$, etc.). We have calculated the radiative corrections to the triple Higgs vertices which we now present. First define parameters similar to the squark mixing parameter C_t:

$$D_t = (A_t - \mu\tan\beta)/(\tilde{t}_1^2 - \tilde{t}_2^2) , \tag{30a}$$

$$E_t = (A_t + \mu\cot\alpha)/(\tilde{t}_1^2 - \tilde{t}_2^2) , \tag{30b}$$

$$F_t = (A_t - \mu\tan\alpha)/(\tilde{t}_1^2 - \tilde{t}_2^2) . \tag{30c}$$

These parameters enter into the couplings of the top squarks to the A, H, and h, respectively. The radiative corrections to the triple Higgs vertices are

$$\lambda_{HAA} = \lambda^0_{HAA} + \Delta\lambda_{HAA} , \tag{31a}$$

$$\lambda_{hAA} = \lambda^0_{hAA} + \Delta\lambda_{hAA} , \tag{31b}$$

$$\lambda_{HHH} = \lambda^0_{HHH} + \Delta\lambda_{HHH} , \tag{31c}$$

$$\lambda_{HHh} = \lambda^0_{HHh} + \Delta\lambda_{HHh} , \tag{31d}$$

$$\lambda_{Hhh} = \lambda^0_{Hhh} + \Delta\lambda_{Hhh} , \tag{31e}$$

$$\lambda_{hhh} = \lambda^0_{hhh} + \Delta\lambda_{hhh} , \tag{31f}$$

where the tree-level couplings are given by

$$\lambda^0_{HAA} = \frac{igZ}{2\cos\theta_W}\cos 2\beta\cos(\beta+\alpha) , \tag{32a}$$

$$\lambda^0_{hAA} = -\frac{igZ}{2\cos\theta_W}\cos 2\beta\sin(\beta+\alpha) , \tag{32b}$$

$$\lambda^0_{HHH} = -\frac{3igZ}{2\cos\theta_W}\cos 2\alpha\cos(\beta+\alpha) , \tag{32c}$$

$$\lambda^0_{HHh} = \frac{igZ}{2\cos\theta_W}[2\sin 2\alpha\cos(\beta+\alpha)+\sin(\beta+\alpha)\cos 2\alpha] , \tag{32d}$$

$$\lambda^0_{Hhh} = -\frac{igZ}{2\cos\theta_W}[\,2\sin 2\alpha\sin(\beta+\alpha) - \cos(\beta+\alpha)\cos 2\alpha] , \tag{32e}$$

$$\lambda^0_{hhh} = -\frac{3igZ}{2\cos\theta_W}\cos 2\alpha\sin(\beta+\alpha) , \tag{32f}$$

and the one-loop corrections are

$$\Delta\lambda_{HAA} = -\frac{igZ}{2\cos\theta_W}\left(\frac{3g^2\cos^2\theta_W}{16\pi^2}\frac{t^4}{W^4}\frac{\sin\alpha\cos^2\beta}{\sin^3\beta}\right)\left(\ln\frac{\tilde{t}_1^2\tilde{t}_2^2}{t^4} + (\tilde{t}_1^2-\tilde{t}_2^2)(D_t^2+C_tE_t)\ln\frac{\tilde{t}_1^2}{\tilde{t}_2^2} + (\tilde{t}_1^2-\tilde{t}_2^2)^2 C_t D_t^2 E_t g_t\right) , \tag{33a}$$

$$\Delta\lambda_{hAA} = -\frac{igZ}{2\cos\theta_W}\left(\frac{3g^2\cos^2\theta_W}{16\pi^2}\frac{t^4}{W^4}\frac{\cos\alpha\cos^2\beta}{\sin^3\beta}\right)\left(\ln\frac{\tilde{t}_1^2\tilde{t}_2^2}{t^4} + (\tilde{t}_1^2-\tilde{t}_2^2)(D_t^2+C_tF_t)\ln\frac{\tilde{t}_1^2}{\tilde{t}_2^2} + (\tilde{t}_1^2-\tilde{t}_2^2)^2 C_t D_t^2 F_t g_t\right) , \tag{33b}$$

$$\Delta\lambda_{HHH} = -\frac{igZ}{2\cos\theta_W}\left(\frac{3g^2\cos^2\theta_W}{16\pi^2}\frac{t^4}{W^4}\frac{\sin^3\alpha}{\sin^3\beta}\right) \times\left[3\ln\frac{\tilde{t}_1^2\tilde{t}_2^2}{t^4}+3(\tilde{t}_1^2-\tilde{t}_2^2)C_tE_t\ln\frac{\tilde{t}_1^2}{\tilde{t}_2^2}+\delta_{HHH}+2\left(\frac{t^2}{\tilde{t}_1^2}[1+(\tilde{t}_1^2-\tilde{t}_2^2)C_tE_t]^3+\frac{t^2}{\tilde{t}_2^2}[1-(\tilde{t}_1^2-\tilde{t}_2^2)C_tE_t]^3-2\right)\right], \tag{33c}$$

$$\Delta\lambda_{HHh} = -\frac{igZ}{2\cos\theta_W}\left(\frac{3g^2\cos^2\theta_W}{16\pi^2}\frac{t^4}{W^4}\frac{\sin^2\alpha\cos\alpha}{\sin^3\beta}\right) \times\left[3\ln\frac{\tilde{t}_1^2\tilde{t}_2^2}{t^4}+(\tilde{t}_1^2-\tilde{t}_2^2)C_t(2E_t+F_t)\ln\frac{\tilde{t}_1^2}{\tilde{t}_2^2}+\delta_{HHh}\right. \left.+2\left(\frac{t^2}{\tilde{t}_1^2}[1+(\tilde{t}_1^2-\tilde{t}_2^2)C_tE_t]^2[1+(\tilde{t}_1^2-\tilde{t}_2^2)C_tF_t]+\frac{t^2}{\tilde{t}_2^2}[1-(\tilde{t}_1^2-\tilde{t}_2^2)C_tE_t]^2[1-(\tilde{t}_1^2-\tilde{t}_2^2)C_tF_t]-2\right)\right], \tag{33d}$$

$$\Delta\lambda_{Hhh} = -\frac{igZ}{2\cos\theta_W}\left(\frac{3g^2\cos^2\theta_W}{16\pi^2}\frac{t^4}{W^4}\frac{\sin\alpha\cos^2\alpha}{\sin^3\beta}\right) \times\left[3\ln\frac{\tilde{t}_1^2\tilde{t}_2^2}{t^4}+(\tilde{t}_1^2-\tilde{t}_2^2)C_t(E_t+2F_t)\ln\frac{\tilde{t}_1^2}{\tilde{t}_2^2}+\delta_{Hhh}\right. \left.+2\left(\frac{t^2}{\tilde{t}_1^2}[1+(\tilde{t}_1^2-\tilde{t}_2^2)C_tE_t][1+(\tilde{t}_1^2-\tilde{t}_2^2)C_tF_t]^2+\frac{t^2}{\tilde{t}_2^2}[1-(\tilde{t}_1^2-\tilde{t}_2^2)C_tE_t][1-(\tilde{t}_1^2-\tilde{t}_2^2)C_tF_t]^2-2\right)\right], \tag{33e}$$

$$\Delta\lambda_{hhh} = -\frac{igZ}{2\cos\theta_W}\left(\frac{3g^2\cos^2\theta_W}{16\pi^2}\frac{t^4}{W^4}\frac{\cos^3\alpha}{\sin^3\beta}\right) \times\left[3\ln\frac{\tilde{t}_1^2\tilde{t}_2^2}{t^4}+3(\tilde{t}_1^2-\tilde{t}_2^2)C_tF_t\ln\frac{\tilde{t}_1^2}{\tilde{t}_2^2}+\delta_{hhh}+2\left(\frac{t^2}{\tilde{t}_1^2}[1+(\tilde{t}_1^2-\tilde{t}_2^2)C_tF_t]^3+\frac{t^2}{\tilde{t}_2^2}[1-(\tilde{t}_1^2-\tilde{t}_2^2)C_tF_t]^3-2\right)\right]. \tag{33f}$$

We have not shown the contributions from b and $\tilde{b}$ which in general are much smaller, and are easily obtained from the above formulas with the proper substitutions. The δ terms in the above formulas are zero for the parameters we have chosen ($Q^2 = U^2$), but they are given in general by the expressions

$$\delta_{HHH} = \delta\left(3(\tilde{t}_1^2-\tilde{t}_2^2)E_t^2\ln\frac{\tilde{t}_1^2}{\tilde{t}_2^2}+3(\tilde{t}_1^2-\tilde{t}_2^2)^2C_tE_t^3g_t\right), \tag{34a}$$

$$\delta_{HHh} = \delta\left((\tilde{t}_1^2-\tilde{t}_2^2)E_t(E_t+2F_t)\ln\frac{\tilde{t}_1^2}{\tilde{t}_2^2} +3(\tilde{t}_1^2-\tilde{t}_2^2)^2C_tE_t^2F_tg_t\right), \tag{34b}$$

$$\delta_{Hhh} = \delta\left((\tilde{t}_1^2-\tilde{t}_2^2)F_t(2E_t+F_t)\ln\frac{\tilde{t}_1^2}{\tilde{t}_2^2} +3(\tilde{t}_1^2-\tilde{t}_2^2)^2C_tE_tF_t^2g_t\right), \tag{34c}$$

$$\delta_{hhh} = \delta\left(3(\tilde{t}_1^2-\tilde{t}_2^2)F_t^2\ln\frac{\tilde{t}_1^2}{\tilde{t}_2^2}+3(\tilde{t}_1^2-\tilde{t}_2^2)^2C_tF_t^3g_t\right), \tag{34d}$$

where

$$\delta = \left(\frac{Q^2-U^2}{\tilde{t}_1^2-\tilde{t}_2^2}\right)^2. \tag{35}$$

IV. PRODUCTION CROSS SECTIONS

The major subprocesses for producing h bosons at pp supercolliders are

$$gg \to h, \tag{36a}$$
$$qq \to qqh, \tag{36b}$$
$$q\bar{q}, gg \to t\bar{t}h, \tag{36c}$$
$$q\bar{q} \to Wh, \tag{36d}$$
$$q\bar{q}, gg \to b\bar{b}h, \tag{36e}$$

where g and q denote gluons and light quarks. There are similar channels for H boson production. To evaluate the hadronic cross sections we use the Harriman-Martin-Roberts-Stirling set B [HMRS(B)] parton distributions [14]. The Q^2 scale is chosen to be $Q^2 = m_h^2$ in (36a), $Q^2 = m_W^2$ in (36b) and $Q^2 = \hat{s}/4$ in the other subprocesses, where $\hat{s}$ is the subprocess c.m. energy squared. In all calculations we use the 3-loop expression for α_s:

$$\alpha_s(Q^2) = \frac{-2}{b_0\ln\frac{Q^2}{\Lambda^2}}\left(1+\frac{2b_1}{b_0^2}\frac{\ln\ln\frac{Q^2}{\Lambda^2}}{\ln\frac{Q^2}{\Lambda^2}}\right) +\frac{4b_1^2}{b_0^4\ln^2\frac{Q^2}{\Lambda^2}}\left[\left(\ln\ln\frac{Q^2}{\Lambda^2}-\frac{1}{2}\right)^2+\frac{b_2b_0}{b_1^2}-\frac{5}{4}\right], \tag{37}$$

where

$$b_0 = -\frac{1}{2\pi}\left(11 - \frac{2f}{3}\right), \tag{38a}$$

$$b_1 = -\frac{1}{4\pi^2}\left(51 - \frac{19f}{3}\right), \tag{38b}$$

$$b_2 = -\frac{1}{64\pi^3}\left(2857 - \frac{5033f}{9} + \frac{325f^2}{27}\right). \tag{38c}$$

The reference mass scales $\Lambda^{(f)}_{\overline{\rm MS}}$ are related by matching the three loop $\alpha_s(Q)$ at the flavor thresholds as in Eq. (8) of Ref. [15]. ($\overline{\rm MS}$ denotes the modified minimal-subtraction scheme.) We choose $\Lambda^{(4)}_{\overline{\rm MS}} = 220\,{\rm MeV}$, which gives $\alpha_s(M_Z^2) = 0.112$, consistent with the measured value $\alpha_s(M_Z^2) = 0.118 \pm 0.008$ [16].

The $gg \to h$ subprocess proceeds principally through t- and b-quark loops and the corresponding $\tilde{t}$- and $\tilde{b}$-squark loops. The squark couplings to the Higgs boson are proportional to the corresponding quark mass; terms which do not depend on the corresponding quark mass cancel. The b and $\tilde{b}$ contributions are only large at large $\tan\beta$ where the $hb\bar{b}$ coupling is enhanced: see Eq. (26).

The $gg \to h(g), gq \to hq$, and $q\bar{q} \to hg$ fusion contributions via the top-quark loop have been evaluated to $\mathcal{O}(\alpha_s^3)$ in Ref. [17]. The result for $m_h < 2m_t$ may be formally expressed as

$$\sigma(pp \to h) = \sigma_0\left(1 + C\frac{\alpha_s}{\pi}\right)\tau_h \frac{d\mathcal{L}^{gg}}{d\tau_H} + \Delta\sigma_{gg} + \Delta\sigma_{gq} + \Delta\sigma_{q\bar{q}}, \tag{39}$$

where σ_0 is the lowest-order cross section and the $\Delta\sigma$ are contributions from $2 \to 3$ subprocesses, $d\mathcal{L}^{gg}/d\tau_h$ is the gg luminosity, $\tau_H = m_h^2/s$, and $C = 11/2 + \pi^2$ at the scale $Q^2 = m_h^2$. Numerically the $\Delta\sigma$ contributions are relatively small and consequently will be neglected. The C term enhances σ_0 by about 50%. The top and stop contributions to σ_0 are calculated using the formulas summarized in Ref. [18]; see also [19].

For large $\tan\beta$ the bottom-quark loop contributions to the lowest-order amplitude are actually larger than those due to the top-quark loop. The QCD corrections for the b-loop case are unknown, so we simply use σ_0, for all quark and squark loop contributions to the $gg \to h$ amplitude. In all the above calculations we take

$$m_s = 0.3, \quad m_c = 1.35, \quad m_b = 4.25, \quad \text{and } m_t = 150 \tag{40}$$

in GeV units (see Ref. [20]).

For the corresponding calculation of H production we use only the σ_0 calculation, since the QCD corrections given in Ref. [17] do not apply for $m_H > 2m_t$. All the quark and squark loop contributions are included in the amplitude.

The pp cross sections for h and H production via gg fusion at the Superconducting Super Collider (SSC) energy $\sqrt{s} = 40\,{\rm TeV}$ are shown in Fig. 6, versus the corresponding Higgs-scalar masses for $\tan\beta = 2$, 30 (solid curves) along with the tree-level predictions (dotted curves). The SM prediction is also shown for comparison.

The $qq \to qqh(H)$ subprocesses proceed principally via $W^+W^- \to h(H)$ fusion with a smaller contribution from $ZZ \to h(H)$ fusion; we shall use the symbol V to denote a generic weak boson W or Z. Figure 7 shows the corresponding pp cross sections at SSC energy. The VVh and VVH vertices contain factors $\sin(\beta-\alpha)$ and $\cos(\beta-\alpha)$ respectively, which reduce each cross section below the corresponding SM cross section; this suppression already occurs at tree level and we see that both h production and especially H production are drastically suppressed relative to SM values (except when the corresponding mass m_h/m_H is near its upper/lower bound.) However, the degree of suppression depends on α, which can suffer large one-loop corrections as seen above. Figure 7

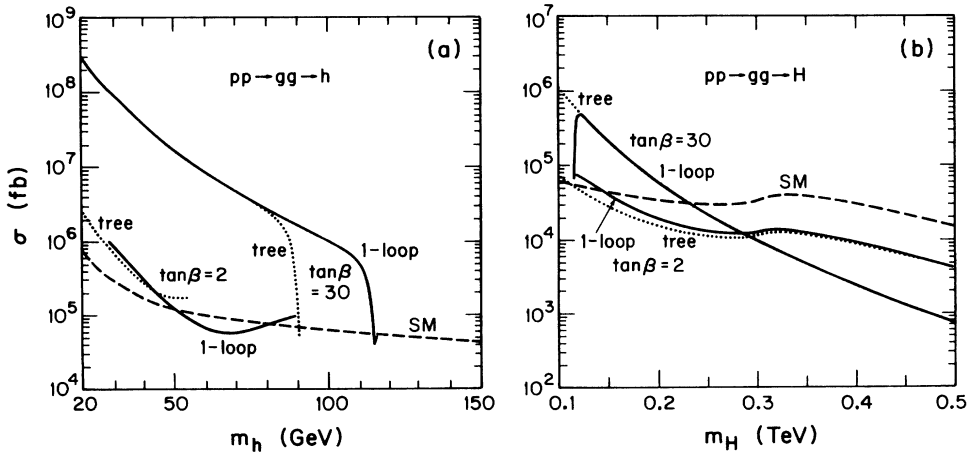

FIG. 6. Production of h and H bosons via $gg \to h(H)$ subprocesses in pp collisions at $\sqrt{s} = 40\,{\rm TeV}$, for the MSSM with the parameter choices of Eqs. (27), (28), (29), and (40) with $\tan\beta = 2$ or 30; (a) $\sigma(pp \to hX)$ vs m_h, (b) $\sigma(pp \to HX)$ vs m_H. Solid curves denote radiatively corrected cross sections, dotted curves denote tree-level results; dashed curves represent SM results.

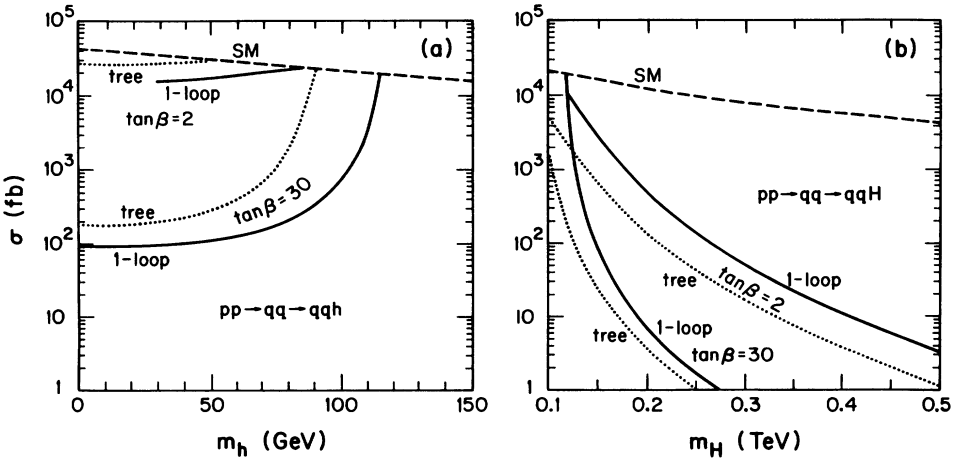

FIG. 7. Production of h and H bosons via $qq \to qqh(H)$ subprocesses in pp collisions at $\sqrt{s} = 40$ TeV, for our parameter choices with $\tan\beta = 2$ or 30; (a) $\sigma(pp \to hX)$ vs m_h, (b) $\sigma(pp \to HX)$ vs m_H. Solid (dotted) curves denote one-loop (tree-level) cross sections; dashed curves represent SM results.

shows that one-loop corrections tend to suppress h production but enhance H production via VV fusion, as expected from our previous discussion of their effects on the underlying hVV and HVV couplings (Sec. III). Unfortunately, from an experimental point of view, it is h production (less suppressed at tree level) that receives further suppression at one-loop level; the small enhancement at one-loop level goes to H production, where it can do little to offset the heavy tree-level suppression that dominates through most of the mass range.

There has been considerable interest [21–25] in subprocesses (36c) and (36d) in connection with searches for a standard-model Higgs boson of intermediate mass $M_Z \lesssim m_H \lesssim 2M_Z$, using the $H_{\rm SM} \to \gamma\gamma$ decay mode [26, 27]. The subprocesses $q\bar{q}, gg \to t\bar{t}h$ involve the $ht\bar{t}$ coupling factors of Eqs. (26) while the subprocess $q\bar{q} \to Wh$ proceeds via the hWW coupling. Figures 8 and 9 show the corresponding pp cross sections at the SSC energy, versus Higgs-boson mass in the intermediate range, considering both h and H production. The $q\bar{q} \to Wh(H)$ subprocess cross section includes a QCD enhancement of $K = 1 + 8\pi/9\alpha_s(\hat{s}/4)$.

In Fig. 8 we see that both h and H production are suppressed at tree level, relative to SM values, except at the upper m_h and lower m_H end points. The one-loop corrections then tend to further suppress h and enhance H production, as expected from our discussion in Sec. III; the final results lie well below the SM curves except when the corresponding mass m_h (m_H) approaches its upper (lower) bound.

The $Wh(H)$ cross sections in Fig. 9 are suppressed relative to the SM in qualitatively the same way as in the $qq \to qqh(H)$ cases in Fig. 7, since the same $VVh(H)$ couplings are involved. Our discussion of Fig. 7 therefore

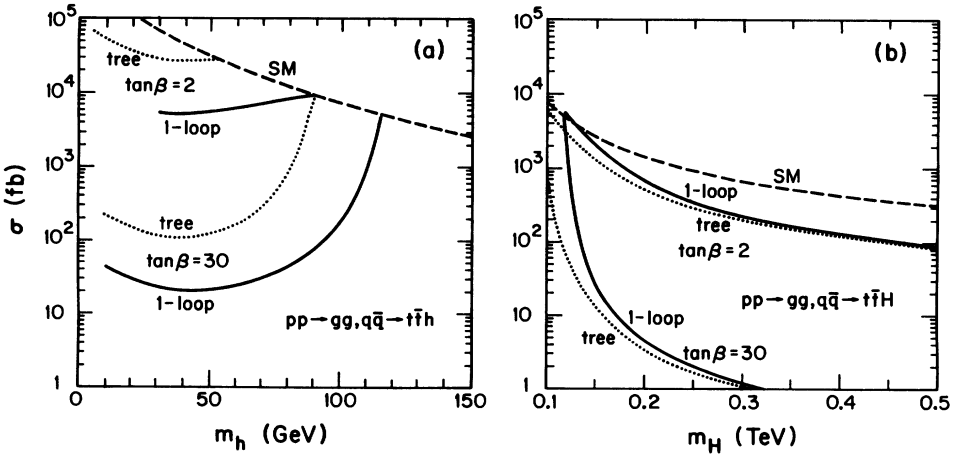

FIG. 8. Production of h and H bosons via $q\bar{q}, gg \to t\bar{t}h(H)$ subprocesses in pp collisions at $\sqrt{s} = 40$ TeV, for our parameter choices with $\tan\beta = 2$ or 30; (a) $\sigma(pp \to ht\bar{t}X)$ vs m_h, (b) $\sigma(pp \to Ht\bar{t}X)$ vs m_H. Solid (dotted) curves denote one-loop (tree-level) results; dashed curves represent SM results.

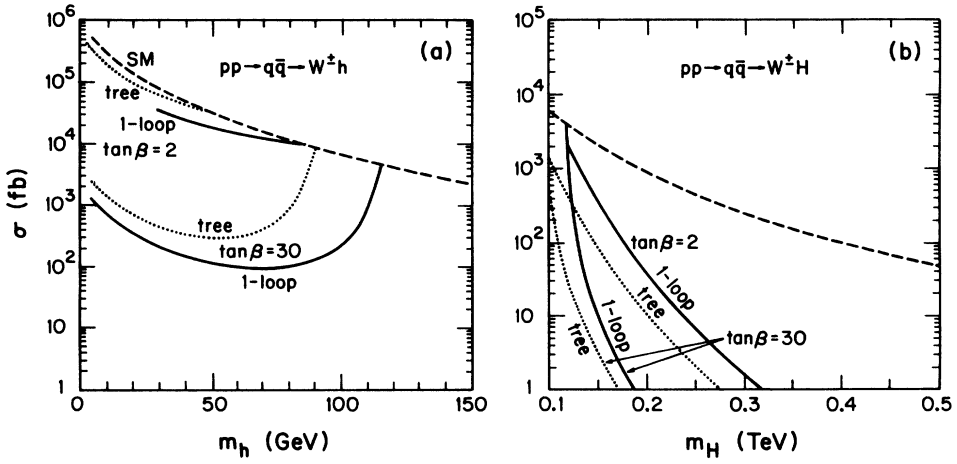

FIG. 9. Production of h and H bosons via $q\bar{q} \to Wh(H)$ subprocesses in pp collisions at $\sqrt{s} = 40$ TeV, for our parameter choices with $\tan\beta = 2$ or 30; (a) $\sigma(pp \to WhX)$ vs m_h, (b) $\sigma(pp \to WHX)$ vs m_H. Solid (dotted) curves denote one-loop (tree-level) results; dashed curves represent SM results.

applies equally to Fig. 9.

Finally we come to the subprocess (36e). It has been pointed out [12] that the tree-level cross section in this channel becomes very large for large $\tan\beta$, due to the $1/\cos\beta$ coupling dependence [see Eq. (26)]. Figure 10 shows the corresponding pp cross section at the SSC energy; the dominant feature is the above enhancement relative to SM expectations, through most of the relevant mass ranges. The radiative corrections add a further enhancement of h production and suppression of H production, due to the shift in α as discussed in Sec. III.

To summarize this section, contributions from the subprocesses (36a)–(36d) that depend on $t\bar{t}$, WW, or ZZ couplings are generally suppressed relative to SM values except in two end-point regions. For given $\tan\beta$, $h(H)$ production approaches SM values when m_h (m_H) approaches its upper (lower) limit; this was to be expected from our general discussion of couplings in Sec. III. In complete contrast, contributions from $b\bar{b}$ couplings via subprocesses (36e) are greatly enhanced above SM values for large $\tan\beta$. We note that LEP data [11] already exclude the range $m_h < 43$ GeV in Figs. 6(a)–10(a). For given $\tan\beta$, this m_h bound implies that a range of m_H near the lower end point is also excluded; however, as we saw in Sec. III, the mixing angle α and hence the H couplings can still approach their end-point values.

V. DECAY BRANCHING FRACTIONS

We focus our attention on the decay branching fractions of h and H, that are modified by the one-loop corrections to the neutral-Higgs-boson mixing angle α. In addition to all tree-level diagrams, we include all quark

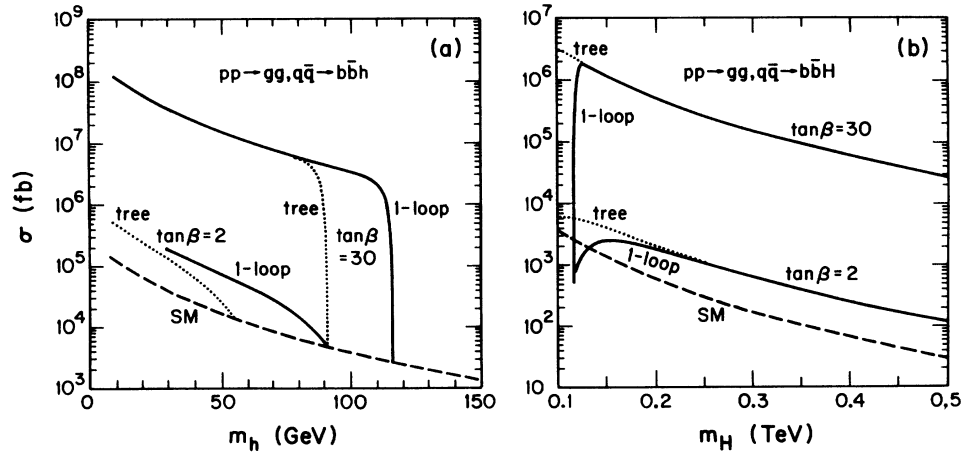

FIG. 10. Production of h and H bosons via $q\bar{q}, gg \to b\bar{b}h(H)$ subprocesses in pp collisions at $\sqrt{s} = 40$ TeV, for our parameter choices with $\tan\beta = 2$ or 30; (a) $\sigma(pp \to b\bar{b}hX)$ vs m_h, (b) $\sigma(pp \to b\bar{b}HX)$ vs m_H. Solid (dotted) curves denote one-loop (tree-level) results; dashed curves represent SM results.

and squark loop contributions, although the t and b loop contributions are dominant. In $h(H) \to \gamma\gamma$ decays we also include the τ-lepton, charged-Higgs-boson and W loop contributions but neglect small chargino loop contributions to avoid the introduction of additional parameters.

In evaluating the $h \to q\bar{q}$ width we include QCD corrections through $O(\alpha_s^2)$, given by [28]

$$\Gamma(h \to q\bar{q}) = \frac{3\sqrt{2}}{2\pi} G_F m_h h_q m_q^2(m_h^2) \left[1 + 5.67\frac{\alpha_s(m_h^2)}{\pi} + (35.94 - 1.36f)\left(\frac{\alpha_s(m_h^2)}{\pi}\right)^2\right] [1 - 4m_q^2(m_q^2)/m_h^2]^{1/2} , \quad (41)$$

where f is the number of active flavors and h_q is the relative coupling from Eq. (26); see Ref. [29] for earlier work. The running quark masses $m_q(Q^2)$ and the strong coupling $\alpha_s(Q^2)$ are evaluated at the scale $Q^2 = m_h^2$, except in the phase-space factor. A similar formula holds for $\Gamma(H \to q\bar{q})$. The electroweak corrections to the $h(H) \to q\bar{q}$ widths [30] are only a few percent for a Higgs-boson mass below 500 GeV, and are not included in our analysis.

The dominant strong-interaction effects give, for the running s, c, b, and t masses,

$$m_q(Q^2) = m_q(m_s^2)\left(\frac{\alpha_s(Q^2)}{\alpha_s(m_s^2)}\right)^{4/9} \frac{F_s(Q^2)}{F_s(m_s^2)} , \quad (42a)$$

$$m_q(Q^2) = m_q(m_c^2)\left(\frac{\alpha_s(Q^2)}{\alpha_s(m_c^2)}\right)^{12/25} \frac{F_c(Q^2)}{F_c(m_c^2)} , \quad (42b)$$

$$m_q(Q^2) = m_q(m_b^2)\left(\frac{\alpha_s(Q^2)}{\alpha_s(m_b^2)}\right)^{12/23} \frac{F_b(Q^2)}{F_b(m_b^2)} , \quad (42c)$$

$$m_q(Q^2) = m_q(m_t^2)\left(\frac{\alpha_s(Q^2)}{\alpha_s(m_t^2)}\right)^{4/7} \frac{F_t(Q^2)}{F_t(m_t^2)} , \quad (42d)$$

in the regions $m_s^2 < Q^2 < m_c^2$ (42a), $m_c^2 < Q^2 < m_b^2$ (42b), $m_b^2 < Q^2 < m_t^2$ (42c), $m_t^2 < Q^2$ (42d), respectively. The running coupling and running masses are matched at the physical q-quark masses $m_q(m_q^2)$. The functions F_q are given through order α_s^2 by [28]

$$F_s(Q^2) = 1 + 0.89\left(\frac{\alpha_s(Q^2)}{\pi}\right) + 1.37\left(\frac{\alpha_s(Q^2)}{\pi}\right)^2 , \quad (43a)$$

$$F_c(Q^2) = 1 + 1.01\left(\frac{\alpha_s(Q^2)}{\pi}\right) + 1.39\left(\frac{\alpha_s(Q^2)}{\pi}\right)^2 , \quad (43b)$$

$$F_b(Q^2) = 1 + 1.17\left(\frac{\alpha_s(Q^2)}{\pi}\right) + 1.50\left(\frac{\alpha_s(Q^2)}{\pi}\right)^2 , \quad (43c)$$

$$F_t(Q^2) = 1 + 1.40\left(\frac{\alpha_s(Q^2)}{\pi}\right) + 1.79\left(\frac{\alpha_s(Q^2)}{\pi}\right)^2 . \quad (43d)$$

The values for $m_q(m_q^2)$ are in Eq. (40).

For the $h \to gg$ width, the top and stop loop contributions are dominant for $\tan\beta = 2$. The QCD correction to the top-quark loop has been recently evaluated [17]. The result is

$$\Gamma(h \to gg) = \frac{G_F\alpha_s^2(m_h^2)}{36\sqrt{2}\pi^3} m_h^3 \{1 + 205/12[\alpha_s(m_h^2)/\pi]^2\}|I|^2 , \quad (44)$$

where the amplitude I is deduced from Appendix A of Ref. [18]. In the squark and b-quark loops the QCD corrections are unknown so we use the lowest-order result. In the $\tan\beta = 30$ case the bottom contributions are large and the QCD corrections are unknown; thus we resort here to the leading-order calculation for all quark loops. We also ignore the QCD corrections to $H \to gg$ decays because the approximations in Ref. [17] are not valid for $m_H > 2m_t$.

For $h \to \gamma\gamma$ decays the QCD correction factor [31] to the top-quark loop amplitude is

$$I_t = I_t^{\text{Born}}\left(1 + C\frac{\alpha_s}{\pi}\right) , \quad (45)$$

where the correction is parametrized by

$$C = \frac{15}{2\tau^2}[\tau + (\tau - 1)\sin^{-2}\sqrt{\tau}] - 6 , \quad \tau = m_h^2/4m_t^2 . \quad (46)$$

The amplitude I_t is given in Appendix A of Ref. [18]. The contributions of the W-boson loop and charged-Higgs-boson loops are evaluated at the Born level, since the QCD corrections are unknown.

We use the tree-level partial width for the $H \to ZA$ decay mode that is kinematically accessible only for a narrow range of masses in our examples ($118 < m_H < 119$ GeV for $\tan\beta = 2$ and $116 < m_H < 117$ GeV for $\tan\beta = 30$). This window becomes larger as m_t increases. The $H \to H^+H^-$ decay is kinematically forbidden for the parameter choices of our analysis.

The $h(H) \to W^+W^-$ and ZZ widths are evaluated at Born level, since electroweak corrections are only a few percent for a Higgs-boson mass below 500 GeV [30].

Figure 11 shows the branching fractions for the principal modes of h decay; the full one-loop corrected values are given (tree-level results are not shown to avoid cluttering the figure). The dominant $b\bar{b}$ and $\tau\bar{\tau}$ fractions remain close to their SM values everywhere. All the other branching fractions shown approach SM values at the upper end point of m_h, but are suppressed below the SM for

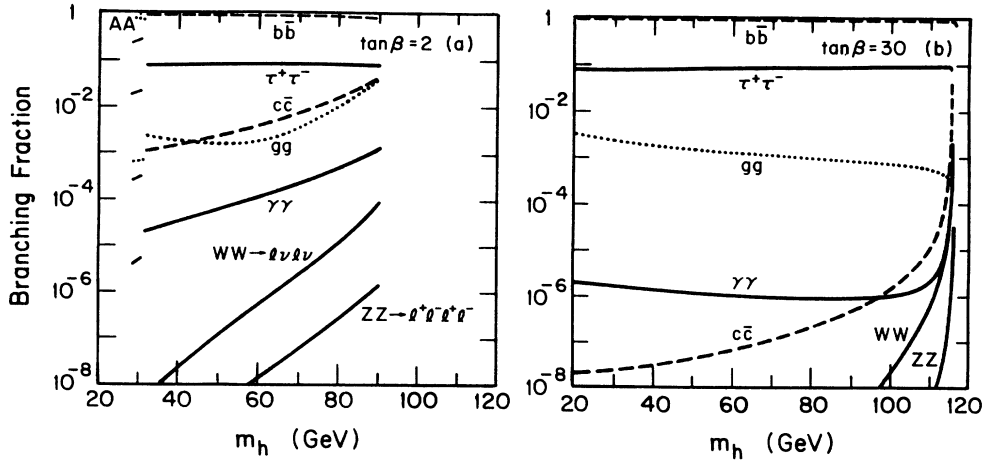

FIG. 11. Decay branching fractions of the lighter CP-even Higgs boson h with typical one-loop radiative corrections: (a) for $\tan\beta = 2$, (b) for $\tan\beta = 30$. The WW and ZZ leptonic decays are summed over $\ell = e, \mu$.

lower m_h (especially for large $\tan\beta$), as we may expect from the behavior of the couplings in Eq. (26). Radiative corrections to the h mass and couplings open the $h \to AA$ decay channel for small m_h and m_A [7]; the $h \to AA$ decay channel is dominant when kinematically accessible, but this region seems to be excluded by the LEP data [11].

The principal branching fractions for H decay are shown in Figs. 12 and 13, at one-loop level. Three general remarks should be made here.

(i) First, consider SM decay modes with $m_H > 2m_t$. At the lower limit of m_H, $\alpha \simeq -\beta$ and the H couplings to fermions have approximately their SM values; as m_H increases, α moves toward $\beta - \pi/2$ and the principal $b\bar{b}$ and $\tau\bar{\tau}$ modes are enhanced by factors of $\tan\beta$ while the other modes are suppressed. Thus $b\bar{b}$ and $\tau\bar{\tau}$ remain the dominant SM modes everywhere while the others are most competitive near the lower m_H end point. It is noteworthy that the $H \to ZZ$ decay mode, that offers the best signatures for a heavy SM Higgs boson, is nowhere important in the MSSM scenario; in the on-shell kinematical region $m_H > 2M_Z$, we have $\alpha \approx \beta - \pi/2$ which suppresses the HZZ coupling factor in Eq. (26).

(ii) Second, the non-SM decay modes $H \to AA$ and $H \to hh$ become important. Formulas for their tree-level partial widths are given in Ref. [1]; they contain the following mixing angle factors [see Eqs. (32a), (32e)]:

$$f_h = \cos 2\alpha \cos(\beta + \alpha) - 2 \sin 2\alpha \sin(\beta + \alpha) , \quad (47a)$$

$$f_A = \cos 2\beta \cos(\beta + \alpha) , \quad (47b)$$

for hh and AA final states, respectively, to which we add the radiative corrections. In Fig. 12(a) where $\tan\beta = 2$, these modes generally dominate over the SM modes, except in the neighborhood of $m_H = 135\,\text{GeV}$ where the hh mode is suppressed by the vanishing of the factor f_h and the AA mode is kinematically forbidden. This poses a problem for all the usual Higgs-boson decay signatures,

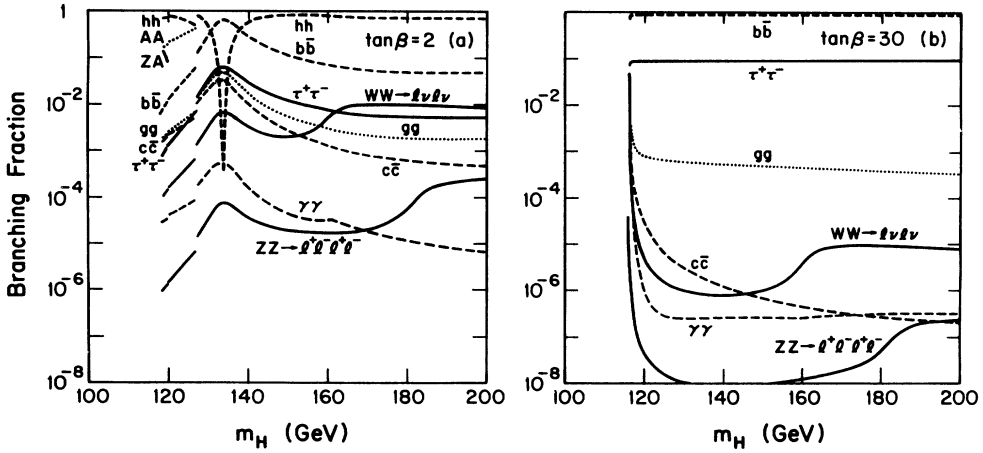

FIG. 12. Decay branching fractions of the heavier CP-even Higgs boson H with typical one-loop radiative corrections for the mass range $m_H < 200$ GeV: (a) with $\tan\beta = 2$, (b) for $\tan\beta = 30$.

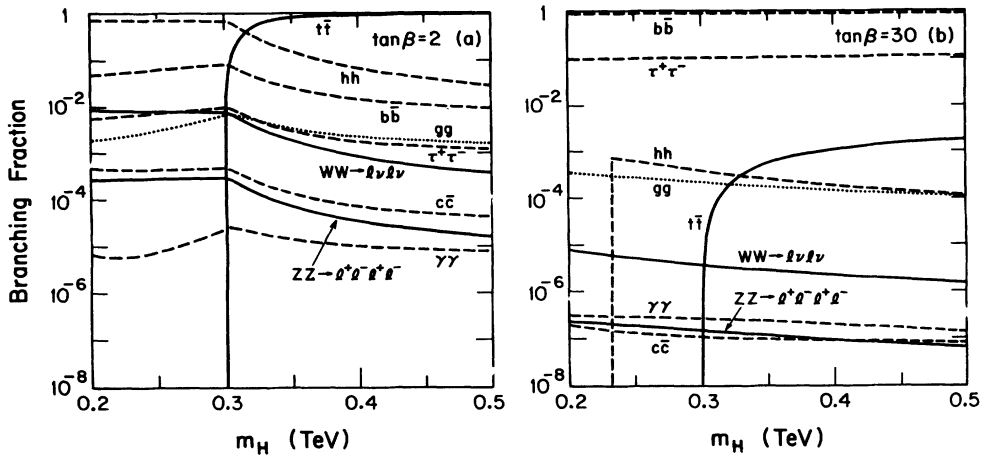

FIG. 13. Decay branching fractions of the heavier CP-even Higgs boson H with typical one-loop radiative corrections for the mass range $200 < m_H < 500$ GeV: (a) with $\tan\beta = 2$, (b) for $\tan\beta = 30$.

that are based on SM decay modes. But for large $\tan\beta$, the case illustrated in Fig. 12(b), new features appear. The threshold condition $m_H > 2m_A$ is satisfied only in a very small island of m_H values near the lower end point; the condition $m_H > 2m_h$ is satisfied both in a similar small island and for high values $m_H \gtrsim 230$ GeV (cf. Fig. 4). These two islands would appear as unintelligible spikes in Fig. 12(b) and have therefore been omitted; note however that here $\alpha \simeq -\pi/2$ and $\beta \simeq \pi/2$, and hence $f_h \simeq f_A \simeq -1$, leaving the hh and AA modes unsuppressed in the islands. For $m_H > 230$ GeV we have small $\alpha \simeq \beta - \pi/2$; hence f_h is small and the $H \to hh$ mode is suppressed [see Fig. 13(b)].

(iii) Third, for $m_H > 2m_t$, the $H \to t\bar{t}$ mode opens up. For small or moderate $\tan\beta$ it completely dominates and suppresses other modes for $m_H > 2m_t$ [cf. Fig. 13(a)], but for large $\tan\beta$ it is swamped by the $H \to b\bar{b}$ and $H \to \tau\bar{\tau}$ modes, as could have been forseen from the formulas in Eq. (26).

VI. SIGNAL RATES

The event rate for a Higgs-boson signal in a given decay channel depends on the product σB of the production cross section σ and the relevant decay branching fraction B. It is helpful to treat separately the contributions from different production mechanisms, since their experimental acceptances may be different; e.g., if we include a W boson in the trigger requirements, subprocesses (36c) and (36d) will be selected preferentially.

Hadroproduced Higgs-boson signals have been extensively studied in the SM framework. We recall that for a neutral scalar in the intermediate-mass range $M_Z < m < 2M_Z$, the major $b\bar{b}$ and $\tau\bar{\tau}$ decay modes are essentially impossible to detect; the most popular candidates here are $\gamma\gamma$ and ZZ^* final states (see, e.g., Refs. [22–27]). For a heavy Higgs boson with $m > 2M_Z$, the detectable final states are $H \to ZZ \to \ell^+\ell^-\ell^+\ell^-$, $H \to ZZ \to \ell^+\ell^-\nu\bar{\nu}$, and $H \to WW \to \ell\bar{\nu}\bar{\ell}\nu$. In projected SM Higgs searches at pp supercolliders, these have been established as promising decay modes; their SM signals can be distinguished from backgrounds [32] but not without difficulty.

Consider first the $\gamma\gamma$ signals from an intermediate mass SM Higgs boson, that we denote $H_{\rm SM}$. The SM branching fractions including radiative corrections can be found in Ref. [33]. The dominant production occurs via the gluon fusion subprocess $gg \to H_{\rm SM} \to \gamma\gamma$. The backgrounds are $q\bar{q}, gg \to \gamma\gamma$ and jet-jet or jet-γ where jet$\to \pi^0$ fakes a photon. In order to extract the signal, excellent mass resolution is necessary, $\delta m_{\gamma\gamma} < 1$–2 GeV, as well as γ-jet discrimination at the 10^{-4} level [25]. These requirements are difficult to achieve with a general purpose detector, but may be realizable with a special purpose detector. The $gg \to t\bar{t}H_{\rm SM}$ and $q\bar{q} \to W^* \to WH_{\rm SM}$ processes [21–25] with $t \to bW$ and $H_{\rm SM} \to \gamma\gamma$ decays offer an improved signature through tagging an isolated high-p_T lepton from $W \to \ell\nu$ decay. This tagged Higgs-boson signal is well above backgrounds from $W\gamma, W\gamma j, Wjj$, etc.; the additional backgrounds from $t\bar{t}\gamma\gamma$ and $b\bar{b}\gamma\gamma$ production appear to be manageable with a mass resolution of a few GeV [22–25]. Thus the $H_{\rm SM} \to \gamma\gamma$ search for the intermediate-mass SM Higgs boson in the $t\bar{t}H_{\rm SM}$ and $WH_{\rm SM}$ channels may be viable, although the event rates are modest (about 14 events from $t\bar{t}H_{\rm SM}$ and 4 events from $WH_{\rm SM}$ at the SSC with 10 fb^{-1} luminosity).

We now discuss the viability of signals for the intermediate-mass MSSM Higgs bosons by comparing calculated production rates with each other and with the SM Higgs-boson rates. In Fig. 14 we show MSSM calculations of σB for $h \to \gamma\gamma$, and $H \to \gamma\gamma$ signals, comparing the contributions from different production mechanisms at the SSC energy $\sqrt{s} = 40$ TeV. Figure 15 shows the signals from $h(H) \to \gamma\gamma$, $qqh(H) \to qq\gamma\gamma$, $h(H) \to ZZ^* \to \ell^+\ell^-\ell^+\ell^-$ (summing over $\ell = e, \mu$ modes), compared with the SM Higgs-boson signal in these channels. Figure 16 shows $h \to \gamma\gamma$ and $H \to \gamma\gamma$ signals in channels that offer potentially better signal/background ratios if lepton tagging of W, t, or b is added (these curves do not include leptonic branching fractions nor tagging efficiencies however). Almost without exception, the MSSM signals fall far below the SM signals. Exceptions occur

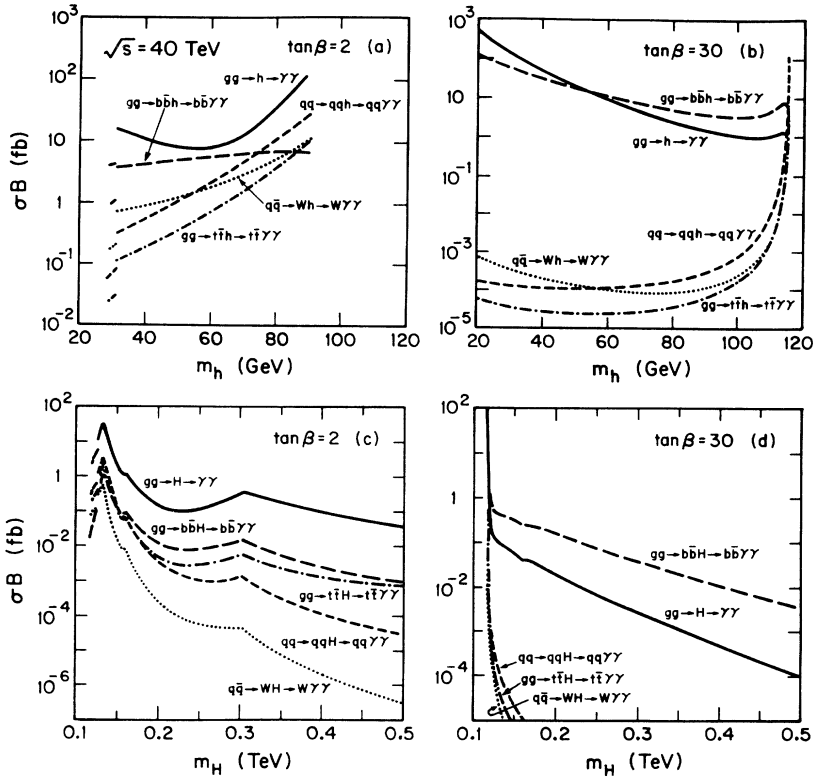

FIG. 14. Signal rates in the two-photon channel; the product σB is shown vs Higgs-boson mass for various production mechanisms at $\sqrt{s} = 40$ TeV: (a) $h \to \gamma\gamma$ signals with $\tan\beta = 2$, (b) $h \to \gamma\gamma$ signals with $\tan\beta = 30$, (c) $H \to \gamma\gamma$ signals with $\tan\beta = 2$, (d) $H \to \gamma\gamma$ signals with $\tan\beta = 30$. LEP data exclude the range $m_h < 43$ GeV [11].

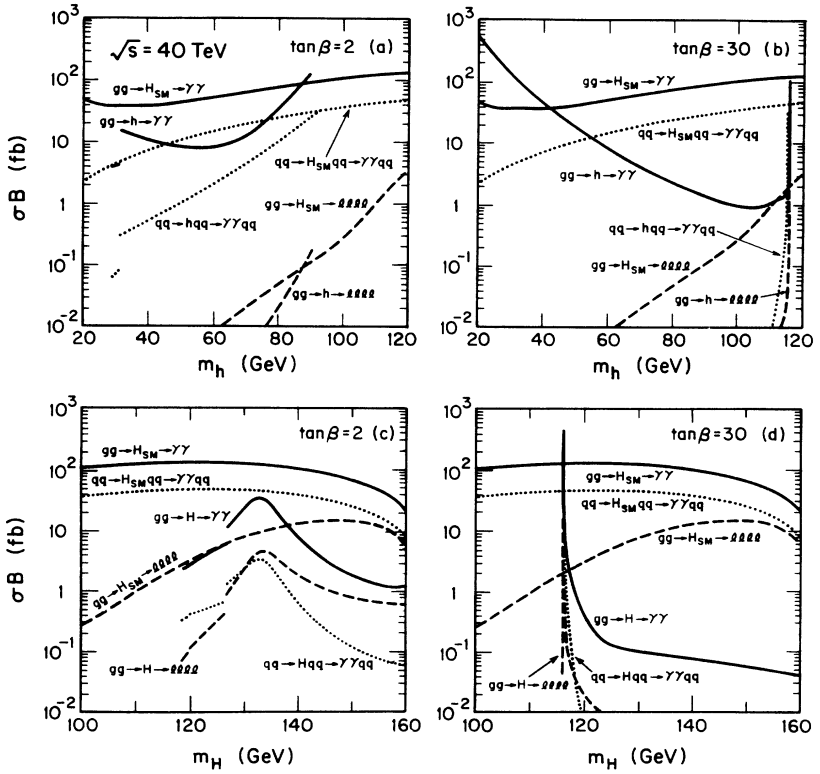

FIG. 15. A comparison of h and intermediate-mass H signals at $\sqrt{s} = 40$ TeV. The product σB is shown vs Higgs-boson mass for $\gamma\gamma$, $qq\gamma\gamma$, and $ZZ^* \to \ell^+\ell^-\ell^+\ell^-$ final states for (a) h signals with $\tan\beta = 2$, (b) h signals with $\tan\beta = 30$, (c) H signals with $\tan\beta = 2$, (d) H signals with $\tan\beta = 30$. LEP data exclude the range $m_h < 43$ GeV [11].

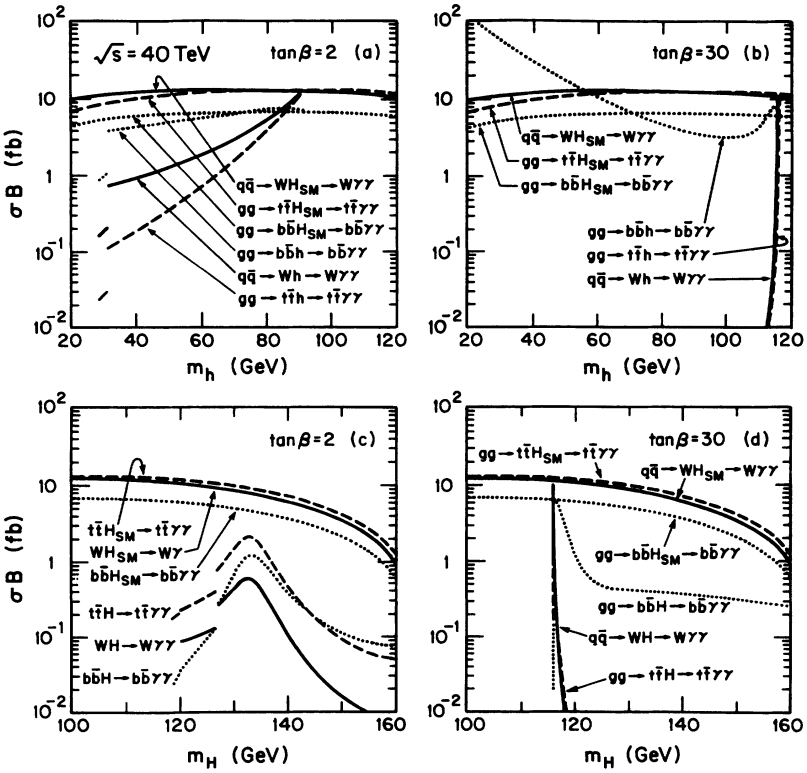

FIG. 16. A comparison of h and H lepton-taggable two-photon signals with SM signals in the intermediate-mass range at $\sqrt{s} = 40$ TeV for (a) h signals with $\tan\beta = 2$, (b) h signals with $\tan\beta = 30$, (c) H signals with $\tan\beta = 2$, (d) H signals with $\tan\beta = 30$. LEP data exclude the range $m_h < 43$ GeV [11].

for all h signals at the upper end point of m_h that we know from Sec. III reduces precisely to the SM case; at this point, small discrepancies between $H_{\rm SM}$ and h curves arise because the latter include more radiative corrections. Also for $b\bar{b}h$ signals there is an enhancement at low m_h and large $\tan\beta$ but most of this region appears to be excluded by the present LEP bound [11] $m_h > 43$ GeV. With H signals the exceptions depend on $\tan\beta$; for large $\tan\beta$ they occur at the lower end point of m_H, while for smaller $\tan\beta$ they occur in a narrow mass band where the competing $H \to hh$ mode is suppressed by the factor f_h.

Figure 17 shows heavy H signals in the most favored "gold plated" $H \to ZZ \to \ell^+\ell^-\ell^+\ell^-$ channels [32]; we see that the MSSM signals are suppressed far below the SM curves, especially for large $\tan\beta$. For $\tan\beta = 2$ and $m_H < 2m_t$, the suppression factor is only 10 and the MSSM signals may in fact still be detectable; for smaller

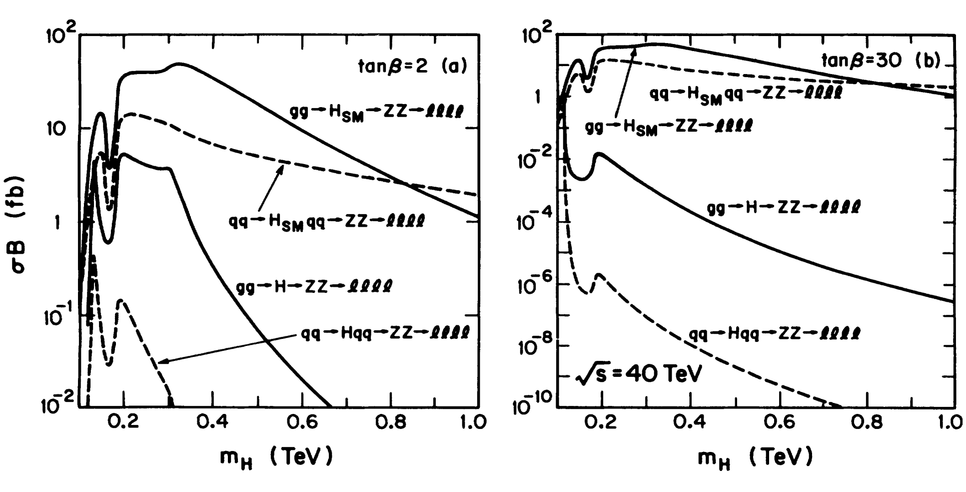

FIG. 17. A comparison of heavy $H \to ZZ \to \ell^+\ell^-\ell^+\ell^-$ signals with SM signals at SSC energy: (a) for $\tan\beta = 2$, (d) for $\tan\beta = 30$.

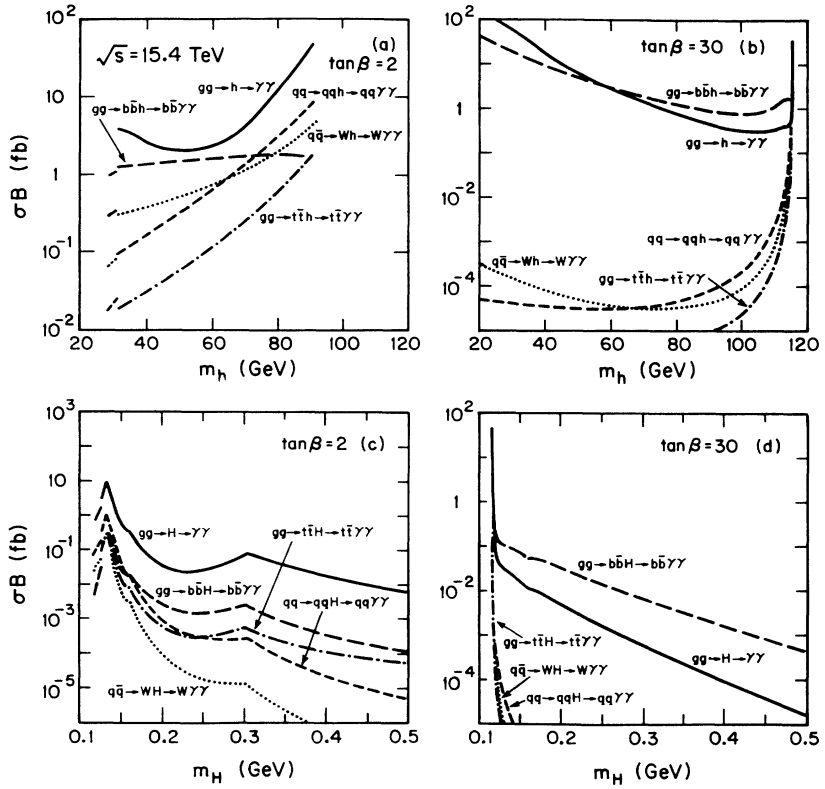

FIG. 18. Same as in Figure 14 but for energy $\sqrt{s} = 15.4$ TeV.

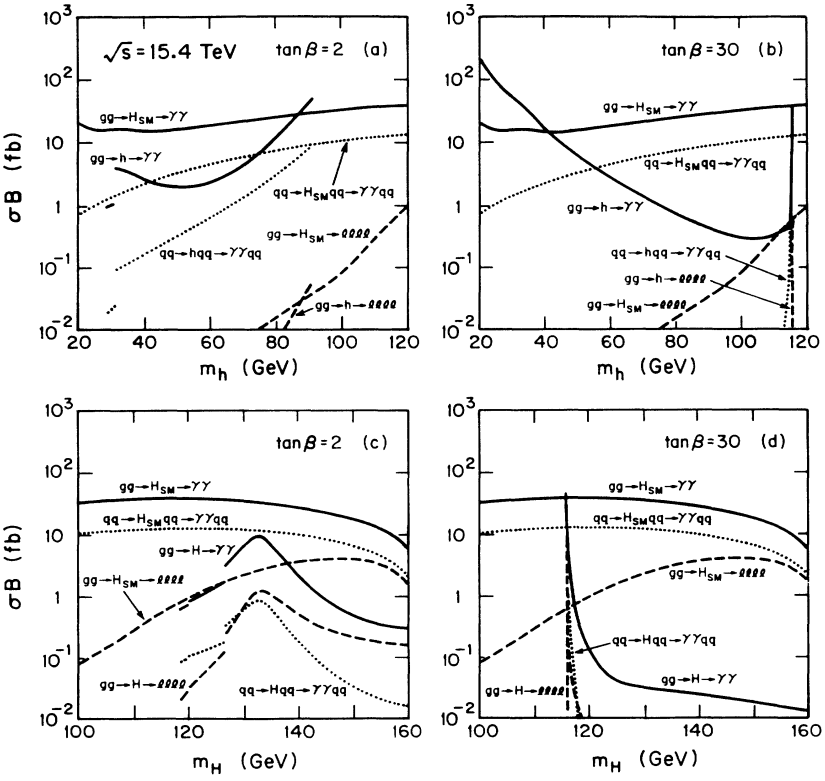

FIG. 19. Same as in Figure 15 but for energy $\sqrt{s} = 15.4$ TeV.

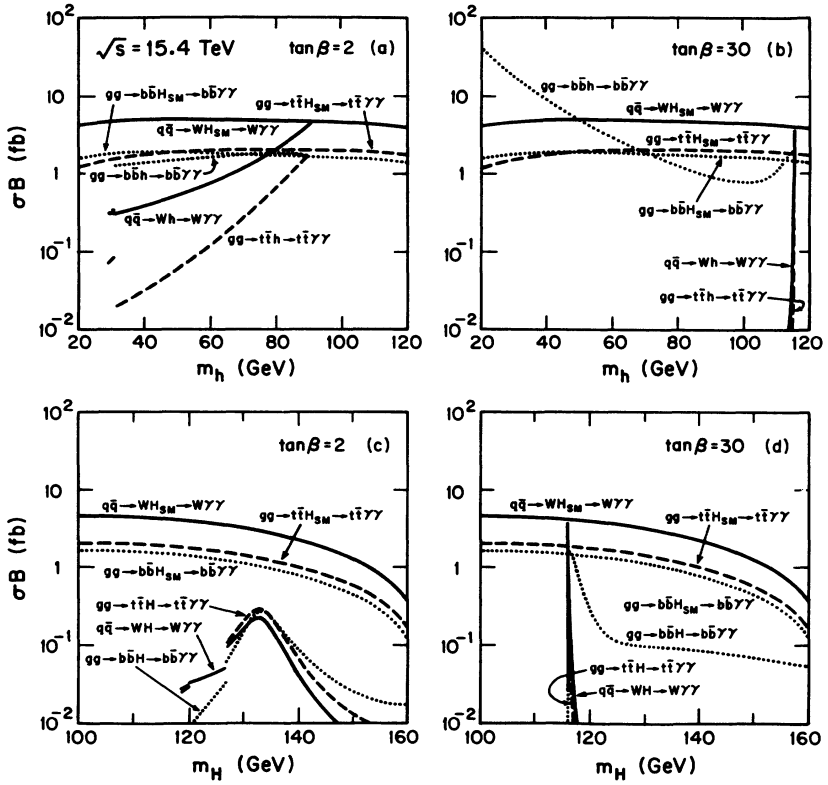

FIG. 20. Same as in Figure 16 but for energy $\sqrt{s} = 15.4$ TeV.

$\tan\beta$ the signals are bigger but for larger m_H or larger $\tan\beta$ the prospects are unpromising. Similar suppression occurs for the $H \to WW \to \ell\bar{\nu}\bar{\ell}\nu$ channel.

Finally, in Figs. 18–21 we show the same h and H signals as in Figs. 14–17 at the lower energy $\sqrt{s} = 15.4$ TeV, corresponding to the Large Hadron Collider (LHC) proposed at CERN.

VII. SUMMARY

Our work is based on the one-loop effective potential approximation in the MSSM, extending the considerations of previous work [2–10]. We have explored some practical consequences of the one-loop radiative corrections for the masses and couplings and hence for the hadroproduction, decay and detectability of the CP-even Higgs eigenstates h and H. A tree-level study of hadroproduced MSSM Higgs-boson signals has been given in Ref. [12]; one-loop corrections appear for the first time in our present work and two concurrent papers, received after our work was completed, in which the $\gamma\gamma$ signals [34] and four-lepton signals [35] are considered. We note that LEP data [11] already appear to exclude the mass range $m_h < 43$ GeV, after one-loop corrections,

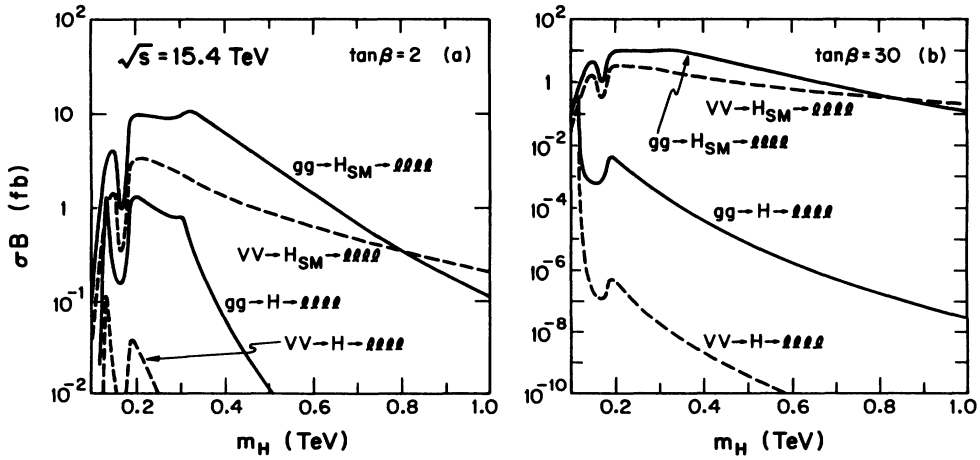

FIG. 21. Same as in Figure 17 but for energy $\sqrt{s} = 15.4$ TeV.

and that future LEP200 searches will probably cover the range $m_h < M_Z$. Our results can be summarized as follows.

(i) The effective potential approximation can be tested in the correction to the mass sum rule. Here the approximation is good for large $\tan\beta$ but can deviate by 15% for $\tan\beta = 2$ near $m_H \simeq m_A \simeq 2m_t$ (see Fig. 2).

(ii) For large $\tan\beta$, one of the h, H masses lies near m_A and the other near a specified value depending quadratically on the top-quark mass and logarithmically on the mean stop mass; see Eq. (21) and Fig. 3. For $m_t = 150\,\text{GeV}$, and mean stop mass of 1 TeV, the fixed Higgs-boson mass eigenvalue is about 115 GeV.

(iii) This fixed mass eigenvalue is a lower bound on m_H and an upper bound on m_h for all $\tan\beta$, if squark mixing is not large.

(iv) For large $\tan\beta$ the masses of all three neutral Higgs bosons h, H, and A can simultaneously fall in the intermediate-mass range $M_Z \leq m \leq 2M_Z$, that is difficult to explore at hadron supercolliders.

(v) The mixing angle α between the CP-even mass eigenstates h and H can be changed appreciably by the one-loop effective potential; for given m_h or m_H, α is shifted to a larger (more negative) value. These changes in the mixing angle α modify the couplings and hence both the production cross sections and decay rates of the CP-even Higgs bosons h and H. Quantitative predictions have been presented for typical SUSY mass scales.

(vi) Near the upper and lower end points of α (for given $\tan\beta$), the couplings of either h or H approach those of the SM Higgs scalar. At the upper end point, h gets precisely the SM couplings and m_h is maximum, while H and A are much heavier. At the lower end point, H gets approximately the SM couplings to $t\bar{t}$, its couplings to WW and ZZ are reduced by approximately $\cos 2\beta$, while its mass m_H is minimum; h and A are then lighter than H. These end point regions occupy a substantial part of the available parameter space; it therefore seems not intrinsically unlikely that α should have a value near such an end point.

(vii) We have evaluated the $O(g^2 m_t^4/m_W^4)$ corrections to the triple Higgs-boson couplings that enter in the decays $h(H) \to AA$ and $H \to hh$.

(viii) Updated branching fractions for h and H have been given to one-loop order.

(ix) For the popular production mechanisms depending on couplings to $t\bar{t}$, WW, or ZZ, the $pp \to h(H)$ cross sections are generally suppressed far below the SM values, except in the end-point regions above.

(x) Couplings to $b\bar{b}$ are exceptional; for large $\tan\beta$ they are greatly enhanced above SM values. Production mechanisms such as Eq. (36e) therefore offer new, nonstandard opportunities to study h or H.

(xi) The final Higgs-boson signals in the $\gamma\gamma$ and $\ell^+\ell^-\ell^+\ell^-$ decay channels, favored for SM Higgs searches, fall far below the SM signals in general; see Figs. 15–17. This is discouraging for searches for the Higgs bosons of the MSSM.

(xii) Exceptions to the general signal suppression occur when m_h is near its upper end point value (some way above M_Z for large $\tan\beta$); here the h couplings approach SM values while H and A are both relatively heavy, so the physics is close to the SM with this specific mass.

(xiii) Other exceptions occur for $H \to \gamma\gamma$ signals, either for large $\tan\beta$ when m_H is at its lower end point or for smaller $\tan\beta$ at a place where competing $H \to hh$ decays are suppressed.

(xiv) The "gold-plated" heavy Higgs signature $H \to ZZ \to \ell^+\ell^-\ell^+\ell^-$ is least suppressed for $m_H < 2m_t$ and small $\tan\beta$ (less than a factor 10 below SM for $\tan\beta < 2$, see Fig. 17). For $2M_Z < m_H < 2m_t$ the SM signal is strong, so the MSSM signal may well be detectable in this region if $\tan\beta \lesssim 2$.

(xv) Apart from these exceptions, however, the prospects for discovering h or H in the MSSM appear much more problematical than for the SM Higgs boson.

ACKNOWLEDGMENTS

We thank Ken-ichi Hikasa and Bernd Kniehl for useful discussions about radiative corrections to Higgs-boson decay widths and thank C. H. Llewellyn Smith, Z. Kunszt and F. Zwirner for communications about our results. This research was supported in part by the University of Wisconsin Research Committee with funds granted by the Wisconsin Alumni Research Foundation, in part by the U.S. Department of Energy under Contract No. DE-AC02-76ER00881, and in part by the Texas National Laboratory Research Commission under Grant No. RGFY9173. Further support was also provided by the U.S. Department of Education under Grant No. P200A80214.

[1] For recent reviews, see J. Gunion, H. Haber, G. Kane, and S. Dawson, *The Higgs Hunter's Guide* (Addison-Wesley, Reading, MA, 1990); X. Tata, in *The Standard Model and Beyond*, edited by J. E. Kim (World Scientific, Singapore, 1991), p. 379.

[2] S. P. Li and M. Sher, Phys. Lett. **140B**, 339 (1984).

[3] J. F. Gunion and A. Turski, Phys. Rev. D **39**, 2701 (1989); **40**, 2325 (1989); **40**, 2333 (1989).

[4] M. S. Berger, Phys. Rev. D **41**, 225 (1990); Ph.D. thesis, Report No. LBL-30564.

[5] Y. Okada, M. Yamaguchi, and T. Yanagida, Prog. Theor. Phys. **85**, 1 (1991); Phys. Lett. B **262**, 54 (1991).

[6] H. Haber and R. Hempfling, Phys. Rev. Lett. **66**, 1815 (1991).

[7] J. Ellis, G. Ridolfi, and F. Zwirner, Phys. Lett. B **257**, 83 (1991); **262**, 477 (1991); A. Brignole *et al.*, Phys. Lett. B **271**, 123 (1991).

[8] R. Barbieri, M. Frigeni, and F. Caravaglios, Phys. Lett. B **258**, 167 (1991); R. Barbieri and M. Frigeni, *ibid.* **258**, 395 (1991).

[9] J. L. Lopez and D. V. Nanopoulos, Phys. Lett. B **266**, 397 (1991).

[10] A. Yamada, Phys. Lett. B **263**, 233 (1991).

[11] M. Davier, in Proceedings of the Joint International Lepton-Photon Symposium and Europhysics Conference on High Energy Physics, Geneva Switzerland, 1991,

edited by S. Hegarty, K. Potter, and E. Quercigh (unpublished); S. L. Wu, in *The Vancovner Meeting—Particles and Fields '91*, Proceedings of the Joint Meeting of the Division of Particles and Fields of the American Physical Society and the Particle Physics Division of the Canadian Association of Physicists, Vancouver, 1991, edited by D. Ayen, D. Bryman, and M. Comyn (World Scientific, Singapore, 1992).

[12] Z. Kunszt and F. Zwirner, in *Proceedings of the ECFA Large Hadron Collider Workshop*, Aachen, Germany, 1990, edited by G. Jarlskog and D. Rein (CERN Report No. 90-10, Geneva, Switzerland, 1990), Vol. II, p. 578.

[13] See for review M. Sher, Phys. Rep. C **179**, 273 (1989).

[14] P. N. Harriman, A. D. Martin, R. G. Roberts, and W. J. Stirling, Phys. Rev. D **42**, 798 (1990); we use solution B, usually denoted HMRS(B).

[15] W. J. Marciano, Phys. Rev. D **29**, 580 (1984).

[16] J. R. Carter, Report No. LP-HEP 91, 1991 (unpublished).

[17] A. Djouadi, M. Spira, and P. M. Zerwas, Phys. Lett. B **264**, 440 (1991).

[18] J. F. Gunion, G. Gamberini, and S. F. Novaes, Phys. Rev. D **38**, 3481 (1988).

[19] T. J. Weiler and T.-C. Yuan, Nucl. Phys. **B318**, 337 (1989).

[20] J. Gasser and H. Leutwyler, Phys. Rep. **87**, 78 (1982); S. Narison, Phys. Lett. B **216**, 191 (1989).

[21] D. Dicus and S. S. D. Willenbrock, Phys. Rev. D **39**, 751 (1989).

[22] J. F. Gunion, Phys. Lett. B **261**, 510 (1991).

[23] W. J. Marciano and F. E. Paige, Phys. Rev. Lett. **66**, 2433 (1991).

[24] R. Kleiss, Z. Kunszt, and W. J. Stirling, Phys. Lett. B **253**, 269 (1991); Z. Kunszt, Z. Trocsanyi, and W. J. Stirling, *ibid.* **271**, 247 (1991).

[25] M. L. Mangano, Report No. SSC-SDC-90-00113 (unpublished); I. Hinchliffe, Report No. LBL-30635 (unpublished); K. Einsweiler (private communication).

[26] J. F. Gunion, G. L. Kane, and J. Wudka, Nucl. Phys. **B299**, 231 (1988).

[27] See *Proceedings of the ECFA Large Hadron Collider Workshop* [12], Vol. II, Sec. A5.

[28] S. G. Gorishny *et al.*, Mod. Phys. Lett. A **5**, 2703 (1990).

[29] E. Braaten and J. Leveille, Phys. Rev. D **22**, 715 (1980); N. Sakai, *ibid.* **22**, 2220 (1980); T. Inami and T. Kubota, Nucl. Phys. **B179**, 171 (1981); T. Inami, T. Kubota, and Y. Okada, Z. Phys. C **18**, 69 (1983); M. Drees and K. Hikasa, Phys. Lett. B **240**, 445 (1990); **262**, 497 (1991).

[30] B. Kniehl, Madison Report No. MAD/PH/655 (unpublished); B. Kniehl, Nucl. Phys. **B357**, 439 (1991).

[31] A. Djouadi, M. Spira, J. J. van der Bij, and P. M. Zerwas, Phys. Lett. B **257**, 187 (1991).

[32] For recent discussions, see V. Barger, K. Cheung, T. Han, J. Ohnemus, and D. Zeppenfeld, Phys. Rev. D **44**, 1426 (1991); **44**, 2701 (1991); U. Baur and N. Glover, Nucl. Phys. **B347**, 12 (1990).

[33] V. Barger, G. Bhattacharya, T. Han, and B. A. Kniehl, Phys. Rev. D **43**, 779 (1991); V. Barger, K. Cheung, B. Kniehl, and R. J. N. Phillips, Report No. MAD/PH/610 (unpublished).

[34] H. Baer, M. Bisset, C. Kao, and X. Tata, Florida State University Report No. FSU-HEP-911104 (unpublished).

[35] J. F. Gunion, R. Bork, H. E. Haber, and A. Seiden, University of California–Davis Report No. UCD-91-29 (unpublished).